

Sparse deep neural networks for modeling aluminum1 electrolysis dynamics

Erlend Torje Berg Lundby^{a,*}, Adil Rasheed^{a,b}, Jan Tommy Gravdahl^a, Ivar Johan Halvorsen^b

^a*Norwegian University of Science and Technology, Department of Engineering Cybernetics, Trondheim, Norway*

^b*SINTEF Digital, Department of Mathematics and Cybernetics, Trondheim, Norway*

Abstract

Artificial neural networks have a broad array of applications today due to their high degree of flexibility and ability to model nonlinear functions from data. However, the trustworthiness of neural networks is limited due to their black-box nature, their poor ability to generalize from small datasets, and their inconsistent convergence during training. Aluminum electrolysis is a complex nonlinear process with many interrelated sub-processes. Artificial neural networks can potentially be well suited for modeling the aluminum electrolysis process, but the safety-critical nature of this process requires trustworthy models. In this work, sparse neural networks are trained to model the system dynamics of an aluminum electrolysis simulator. The sparse model structure has a significantly reduction in model complexity compared to a corresponding dense neural network. We argue that this makes the model more interpretable. Furthermore, the empirical study shows that the sparse models generalize better from small training sets than dense neural networks. Moreover, training an ensemble of sparse neural networks with different parameter initializations show that the models converge to similar model structures with similar learned input features.

Keywords: Aluminum electrolysis, Sparse neural networks, Data-driven modeling, Nonlinear dynamics, Ordinary differential equations

1. Introduction/ motivation

Aluminum is extracted from the electrolytic Hall-Héroult process. In this process, alumina (Al_2O_3) is dissolved in cryolite (Na_3AlF_6) and then reduced to aluminum. The reaction is driven by a line current that is sent through the electrolytic bath [1]. The dynamics of the aluminum electrolysis process contain nonlinearities and interrelated sub-processes which are challenging to model. Accurate dynamic models are crucial for optimizing product quality and energy consumption. Furthermore, the harsh environment of aluminum electrolysis cells requires extra effort to ensure safe operation. To this end, research efforts have focused on modeling the Hall-Héroult process accurately. Most of the models developed until recently falls in the first principle physics-based models (PBM). For example, authors in [2] developed a model of mass and energy balance based on the first law of thermodynamics. The resulting model includes, among other things, a complete control volume analysis, an extensive material balance, a 3D finite element model (FEM) for modeling resistance in the cell lining and shell, and Computational Fluid Dynamics (CFD) model for calculating gas velocity streamlines. In [3], a multi-scale, multi-physics modeling framework including magneto-hydrodynamics, bubble flow, thermal convection, melting and solidification based on a set of chemical reactions was developed. These kinds of PBMs, although highly interpretable, cannot capture all the complex dynamics of the aluminum electrolysis due to the fact that they have numerous assumptions, incomplete physics, and uncertainties in the input parameters. For example, the magneto-hydrodynamic phenomena or the reactivity and species concentration

*Corresponding author

Email addresses: erlend.t.b.lundby@ntnu.no (Erlend Torje Berg Lundby), adil.rasheed@ntnu.no (Adil Rasheed), jan.tommy.gravdahl@ntnu.no (Jan Tommy Gravdahl), Ivar.J.Halvorsen@sintef.no (Ivar Johan Halvorsen)

distribution are phenomena that are difficult to model [4]. Thus these first-principle model's predictions might deviate significantly from observation.

In recent year owing to the availability of copious amount of data, cheap computational resources, and major advancement in the algorithms, Data-Driven Modeling (DDM) is coming up as an attractive alternative to PBM. The DDM has the potential to accurately model even the poorly understood complex phenomena (mentioned earlier) directly from the data. As a result, a broad array of scientific communities explore their applicability in many engineering applications. Some examples are the use of neural networks to model simulated dynamics of a pressurized water nuclear reactor [5], identification of the dynamics of the production and purification process of bioethanol [6], prediction of chemical reactions [7]. Authors in [8] demonstrated convincingly how DDM outperforms PBM in the absence of the full understanding of physics. However, despite their advantages they suffer from certain shortcomings [9]; they are difficult to interpret, difficult to generalize to solve previously unseen problems, and unstable to train. These are important shortcomings to overcome before the models can be used in high stake applications. We discuss each of these briefly.

Interpretability: This can be defined as the ability of a model to express itself in human interpretable form [10]. A simple model like linear regression having very few trainable parameters can be a good example of an interpretable model. However, a DNN, which can be seen as a complex version of linear regression, and constituting of millions of trainable parameters can be extremely difficult or almost impossible to interpret. Reducing the complexity of DNN models can lead to more interpretable models.

Generalizability: This refers to the models' ability to predict outcome values for unseen data from the same distribution as the training data. Highly complex models are prone to overfitting, meaning that they do not generalize to areas of the input space that training data do not cover. DNN models have shown promising results in prediction accuracy by processing large amounts of data. However, in many complex physical systems, such as aluminum electrolysis, the cost, and challenges of data acquisition limit the training data to partial information about the system dynamics. As a result, many DNN models fail to generalize from limited data, and will provide inaccurate predictions in regions poorly represented by the training data. Reducing the complexity of the DNN can increase the generalizability of the model.

Stability: The training of DNN requires solving an optimization problem where a cost function dependent on thousands or even million of parameters is minimized. Depending upon the complexity of the problems multiple minima can be encountered during the optimization, and the task of converging to the global minima gets increasingly difficult with the number of parameters. By stability in the context of the current work we mean that the optimization leads to a reasonable minima which even if not global is close to it. To the contrary an unstable DNN will be the one where the optimization process gets stuck in a bad local minima.

Combining PBM and DDM in a hybrid modeling approach to address these shortcomings is emerging for a wide range of scientific applications [9]. In [8], the equations known from PBM are augmented by a corrective source term generated by a DNN. In [11], the estimate calculated by a PBM is subtracted from coarse measurements of the metal height in an aluminum electrolysis simulator to find residual measurements. These residual measurements are used by a compressed sensing algorithm to model the unknown disturbance signal of the dynamics. In [12], it is proposed a novel hybrid modeling approach called Physics Informed Neural Network (PINN). PINN utilizes known first principle knowledge expressed in partial differential equations and their corresponding boundary conditions to regularize a neural network that is trained to estimate certain variables. Authors of [13] introduces a method called Physics Guided Machine Learning (PGML). The main idea is to augment simplified theories relevant to the dynamics of the system that is modeled with the learning process of the resulting hybrid DNN model. The simplified theories are considered as features in the resulting model. These features are added to intermediate layers in the neural network architecture rather than to the input layer in order to emphasize their importance. As most of the examples above illustrates, neural networks are often highly important in hybrid models. While hybrid models themselves addresses the shortcomings mentioned above, DNNs utilized in hybrid models still suffer from them. This article focuses on addressing interpretability, generalizability and training stability of DNNs used in a purely DDM manner. This can also highly benefit hybrid models.

In the aluminum electrolysis process, DNNs have been applied to predict essential variables that are difficult to mea-

sure continuously. In [14] and [15] neural networks were used to predict the temperature and the concentration of alumina, aluminum fluoride, and calcium fluoride in the bath. In [16], neural networks were used to model the carbon anode properties as a function of physical and chemical properties. Despite the cited works and many more available in the existing literature, issues related to interpretability, generalizability and training stability of DNN models in the context of the aluminum electrolysis process remains unaddressed.

To this end, in the current article, we apply the sparsity promoting ℓ_1 regularizer on the weights of each layer in DNN models that predict the states in the aluminum electrolysis. The regularization pushes most of the weights to zero, thus reducing the complexity drastically. We demonstrate that the resulting sparse models have increased interpretability, generalizability and training stability.

The article is structured as follows. Section 2 presents the relevant theory for the work in the case study. Section 3 presents the method applied in the paper and the experimental setup of the simulator for data generation. In section 4, the results are presented and discussed. Finally, in section 5, conclusions are given, and potential future work is presented.

2. Theory

2.1. Deep neural networks (DNN)

A DNN is a supervised machine learning algorithm [17] that can be denoted by

$$\mathbf{y} = \hat{\mathbf{f}}(\mathbf{x}; \boldsymbol{\theta}), \quad (1)$$

where $\mathbf{y} \in \mathbb{R}^s$ is the output vector of the network model and s is the length of the output vector of the model. $\mathbf{x} \in \mathbb{R}^d$ is the input vector to the network model, and d is the input dimension. Here, $\boldsymbol{\theta} \in \mathbb{R}^p$ denotes all trainable parameters in the network model. p is the number of parameters. Each layer $j+1$ operates on the output vector from the previous layer $\mathbf{Z}^j \in \mathbb{R}^{L_j}$ and outputs a vector $\mathbf{Z}^{j+1} \in \mathbb{R}^{L_{j+1}}$:

$$\mathbf{Z}^{j+1} = \sigma(\mathbf{W}^{j+1}\mathbf{Z}^j + \mathbf{b}^{j+1}). \quad (2)$$

$\mathbf{W}^{j+1} \in \mathbb{R}^{L_{j+1} \times L_j}$ is called the weight matrix, and $\mathbf{b}^{j+1} \in \mathbb{R}^{L_{j+1}}$ is the called the bias vector of layer $j+1$. $\boldsymbol{\theta} = \{\boldsymbol{\theta}^1, \dots, \boldsymbol{\theta}^{j+1}, \dots\}$, and $\boldsymbol{\theta}^{j+1} = \{\mathbf{W}^{j+1}, \mathbf{b}^{j+1}\}$. σ is a non-linear activation function. That is,

$$\begin{aligned} \sigma(\mathbf{W}^{j+1}\mathbf{Z}^j + \mathbf{b}^{j+1}) &= (\sigma(W_1^{j+1}\mathbf{Z}^j + b_1^{j+1}), \dots, \\ &\quad \sigma(W_i^{j+1}\mathbf{Z}^j + b_i^{j+1}), \dots, \sigma(W_{L_{j+1}}^{j+1}\mathbf{Z}^j + b_{L_{j+1}}^{j+1}))^T. \end{aligned} \quad (3)$$

W_i^{j+1} are the row vectors of the weight matrix \mathbf{W}_{j+1} and b_i^{j+1} , $i = 1, \dots, L_{j+1}$ are the entries of the bias vector \mathbf{b}^{j+1} . Thus, the activation function calculates the output of each neuron in layer $j+1$ as a nonlinear function of the weighted sum of outputs from the neurons in the previous layer plus a bias. Each neuron outputs one value, and the weight in the consecutive layer determines the importance of the output of each neuron in the current layer. The nonlinear activation function σ can, for example, be the sigmoid function, hyperbolic tangent function or the binary step function to mention a few. For the last decade or so, the popularity of the piece-wise linear (PWL) activation function Rectified Linear Unit (ReLU) has grown exponentially. This is in part due to its computational simplicity, representational sparsity and non-vanishing gradients. The ReLU activation function is given by:

$$\sigma(z) = \max\{0, z\}. \quad (4)$$

ReLU is the only activation function used in the current work.

2.2. Sparse neural networks and regularization

Dense neural networks are often overparameterized models, meaning that they have more parameters than can be estimated from the data and thus often suffer from overfitting. In [18], it is shown empirically that randomly initialized dense neural networks contain subnetworks that can improve generalization compared to the dense networks. These

subnetworks, characterized by significantly fewer non-zero trainable parameters than their dense counterpart, are called sparse neural networks. Their utility can further be seen in terms of increased computational performance for inference and training, and increased storage and energy efficiency. Typically large-scale models that require millions to billions of parameters and arithmetic operations can highly benefit from such sparsification. To conclude sparsification of complex models will lead to simpler models which are relatively easier to interpret, generalize, and train.

Among the methods that can be used to sparsify a complex network, regularization techniques are the most popular ones. In regularization, penalty terms $R(\mathbf{w})$ defined on the weights are added to the cost function C :

$$C(\mathbf{x}_i, \mathbf{y}_i, \boldsymbol{\theta}) = L(\mathbf{y}_i, \hat{\mathbf{f}}(\mathbf{x}; \boldsymbol{\theta})) + \lambda R(\mathbf{w}). \quad (5)$$

The vector $\boldsymbol{\theta} = \{\mathbf{w}, \mathbf{b}\}$ denotes the adaptable parameters, namely the weights \mathbf{w} and biases \mathbf{b} in the network model. Furthermore, $\{(\mathbf{x}_i, \mathbf{y}_i)\}_{i=1}^N$ is the training data, $L(\cdot, \cdot)$ is a proper loss function and the positive scalar coefficient λ is a hyperparameter to weight the terms $L(\cdot, \cdot)$ and $R(\cdot)$. The standard choice of loss function $L(\cdot, \cdot)$ for regression tasks is the Mean Squared Error (MSE). In the training process, the cost function is minimized to find optimal values of the parameters:

$$\boldsymbol{\theta}^* = \operatorname{argmin}_{\boldsymbol{\theta}} \left\{ \frac{1}{N} \sum_{i=1}^N C(\mathbf{x}_i, \mathbf{y}_i, \boldsymbol{\theta}) \right\}. \quad (6)$$

The most intuitive sparsity promoting regularizer is the ℓ_0 norm, often referred to as the sparsity norm:

$$R_{\ell_0}(\mathbf{w}) = \|\mathbf{w}\|_0 = \sum_i \begin{cases} 1 & w_i \neq 0, \\ 0 & w_i = 0. \end{cases} \quad (7)$$

The ℓ_0 norm counts the number of nonzero weights. Unfortunately, the ℓ_0 norm has several drawbacks that make it less suitable for optimization. The ℓ_0 norm is nondifferentiable and sensitive to measurement noise. Furthermore, in terms of computational complexity, the problem of ℓ_0 norm is shown to be NP-hard[19]. The ℓ_1 norm is a convex relaxation of the ℓ_0 norm, and is given by:

$$R_{\ell_1}(\mathbf{w}) = \|\mathbf{w}\|_1 = \sum_i |w_i|. \quad (8)$$

Due to its geometrical characteristics, ℓ_1 minimization is sparsity promoting. However, the ℓ_1 norm usually does not reduce the weights to zero but rather to very small magnitudes. Thus, magnitude pruning can be applied after ℓ_1 minimization to achieve true sparse models.

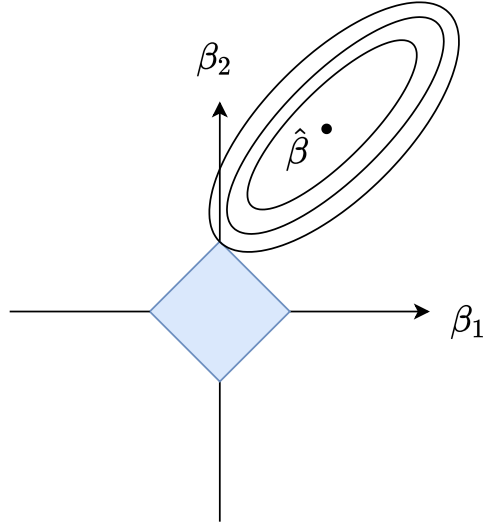


Figure 1: Illustration of ℓ_1 regularization. β_1 and β_2 are the model parameters. $\hat{\beta}$ is the MSE estimate. The ellipses show the contours of the error from the MSE estimate. The blue diamond illustrates the ℓ_1 constraints.

Fig. 1 illustrates how ℓ_1 regularization constraints the parameters to a sparse solution. In this case β_1 is pushed towards zero.

2.3. Region bounds for PWA neural networks

The complexity of neural networks with Piecewise Affine (PWA) activation functions such as ReLU can be analyzed by looking at how the network partitions the models' input space to an exponential number of linear response regions [20, 21]. For each region in the input space, the PWA neural network has a linear response for the output. Authors in [22] present asymptotic upper and lower bounds for maximum number of regions for a DNN with ReLU activation:

$$\begin{aligned} \text{Lower : } & \Omega\left(\left(\frac{n}{d}\right)^{(L-1)d} n^d\right), \\ \text{Upper : } & O(n^{dL}). \end{aligned} \quad (9)$$

d is the input dimension, L is the number of hidden layers, and n is the number of activation functions or neurons in each layer. The bounds in Eq. (9) are valid for networks with the same number of neurons in each layer. The bounds for networks with an uneven number of neurons show similar exponential results and are thus not included for convenience. Eq. (9) illustrates the exponential relation between the input dimension, number of neurons, and the depth of the network. For realistic amounts of data sampled from a physical system, the number of linear regions that a relatively small dense neural network partition the input space into exceeds the sampled data by several orders of magnitude. Thus, in order to generalize to larger areas of the models' input space, the number of regions needs to be reduced drastically. This motivates sparsifying the model.

2.4. Simulation model

The simulation model used in this article is based on the mass and energy balance of an aluminum electrolysis cell. The derivation of the model is found in the Appendix A. In this section, the simulation model is put in a state space form, where constants, system states, and control inputs are denoted by symbols k_i , x_i , or u_i respectively. The simulation model can be expressed as a nonlinear system of ODE's with 8 states $\mathbf{x} \in \mathbb{R}^8$ and 5 inputs $\mathbf{u} \in \mathbb{R}^5$ on the form:

$$\dot{\mathbf{x}} = f(\mathbf{x}, \mathbf{u}), \quad (10)$$

where $\dot{\mathbf{x}} \in \mathbb{R}^8$ is the time derivative of the states \mathbf{x} , and $f(\mathbf{x}, \mathbf{u})$ is a nonlinear function. Table 1 presents the mapping from physical quantities to variables.

Table 1: Table of states and inputs

Variable	Physical meaning	Unit
x_1	mass side ledge	kg
x_2	mass Al_2O_3	kg
x_3	mass AlF_3	kg
x_4	mass Na_3AlF_6	kg
x_5	mass metal	kg
x_6	temperature bath	°C
x_7	temperature side ledge	°C
x_8	temperature wall	°C
u_1	Al_2O_3 feed	kg
u_2	Line current	kA
u_3	AlF_3 feed	kg
u_4	Metal tapping	kg
u_5	Anode-cathode distance	cm

The nonlinear functions in Eqs. 11) - (15 that partly describes the dynamics of the system states are defined in advance of presenting the system dynamics in order to simplify the expressions in Eq. 10:

$$g_1 = 991.2 + 1.12pr_{x_3} - 0.13pr_{x_3}^{2.2} + 0.061pr_{x_3}^{1.5} - \frac{7.93pr_{x_2}}{1 + pr_{x_3}(0.094 - 0.0017pr_{x_3} - 0.0023pr_{x_2})} \quad (11)$$

$$g_2 = \exp(2.496 - \frac{2068.4}{273 + x_6} - 2.07c_{x_2}) \quad (12)$$

$$g_3 = 0.531 + 6.958 \cdot 10^{-7}u_2 - 2.51 \cdot 10^{-12}u_2^2 + 3.1 \cdot 10^{-18}u_2^3 + \frac{0.43 - 0.14(pr_{x_2} - pr_{x_{2,crit}})}{1 + 7.35(pr_{x_2} - pr_{x_{2,crit}})} \quad (13)$$

$$g_4 = \frac{0.5517 + 3.8168 \cdot 10^{-6}u_2}{1 + 8.271 \cdot 10^{-6}u_2} \quad (14)$$

$$g_5 = \frac{3.8168 \cdot 10^{-6} \cdot g_3 \cdot g_4 \cdot u_2}{g_2(1 - g_3)} \quad (15)$$

$$(16)$$

g_1 is the liquidus temperature T_{liq} , g_2 is the electrical conductivity κ from Eq. (A.33), g_3 is the bubble coverage ϕ from Eq. A.37, g_4 is the bubble thickness d_{bub} from Eq. (A.36) and g_5 is the bubble voltage drop U_{bub} . Notice that:

$$c_{x_2} = \frac{x_2}{x_2 + x_3 + x_4}$$

$$c_{x_3} = \frac{x_3}{x_2 + x_3 + x_4}$$

$$pr_{x_2} = 100 \cdot c_{x_2}$$

$$pr_{x_3} = 100 \cdot c_{x_3}$$

With the nonlinear functions $g_1, \dots g_5$ described, the state space equations in Eq. 10 is described by the following:

$$\dot{x}_1 = \frac{k_1(g_1 - x_7)}{x_1 k_0} - k_2(x_6 - g_1) \quad (17)$$

$$\dot{x}_2 = u_1 - k_3 u_2 \quad (18)$$

$$\dot{x}_3 = u_3 - k_4 u_1 \quad (19)$$

$$\dot{x}_4 = -\left(\frac{k_1(g_1 - x_7)}{x_1 k_0} - k_2(x_6 - g_1)\right) + k_5 u_1 \quad (20)$$

$$\dot{x}_5 = k_6 u_2 - u_4 \quad (21)$$

$$\begin{aligned} \dot{x}_6 = & \frac{\alpha}{x_2 + x_3 + x_4} \left[u_2 \left(g_5 + \frac{u_2 u_5}{2620 g_2} \right) \right. \\ & - k_9 \frac{x_6 - x_7}{k_{10} + k_{11} k_0 x_1} \\ & \left. - \left(k_7(x_6 - g_1)^2 - k_8 \frac{(x_6 - g_1)(g_1 - x_7)}{k_0 x_1} \right) \right] \end{aligned} \quad (22)$$

$$\begin{aligned} \dot{x}_7 = & \frac{\beta}{x_1} \left[- \left(k_{12}(x_6 - g_1)(g_1 - x_7) \right. \right. \\ & - k_{13} \frac{(g_1 - x_7)^2}{k_0 x_1} \\ & \left. \left. + \frac{k_9(g_1 - x_7)}{k_{15} k_0 x_1} - \frac{k_9(x_7 - x_8)}{k_{14} + k_{15} k_0 x_1} \right) \right] \end{aligned} \quad (23)$$

$$\dot{x}_8 = k_{17} k_9 \left(\frac{x_7 - x_8}{k_{14} + k_{15} k_0 \cdot x_1} - \frac{x_8 - k_{16}}{k_{14} + k_{18}} \right) \quad (24)$$

3. Method and experimental setup

3.1. Sparsity promoting regularization

In this article, sparse DNN models are utilized to predict state variables in an aluminum electrolysis simulator. All the weight matrices in a DNN model are ℓ_1 regularized to impose sparsity on the model. Fig. 2 illustrates how weights

are enumerated according to their input and output nodes. Layer j has i nodes and layer $(j + 1)$ has r nodes. Layer $j = 0$ corresponds to the input layer, and consist of measured or estimated states $\mathbf{x}(t)$ and control inputs $\mathbf{u}(t)$ at time step t . The output layer consist of the estimated time derivatives of the states $\dot{\mathbf{x}}(t)$ at time step t .

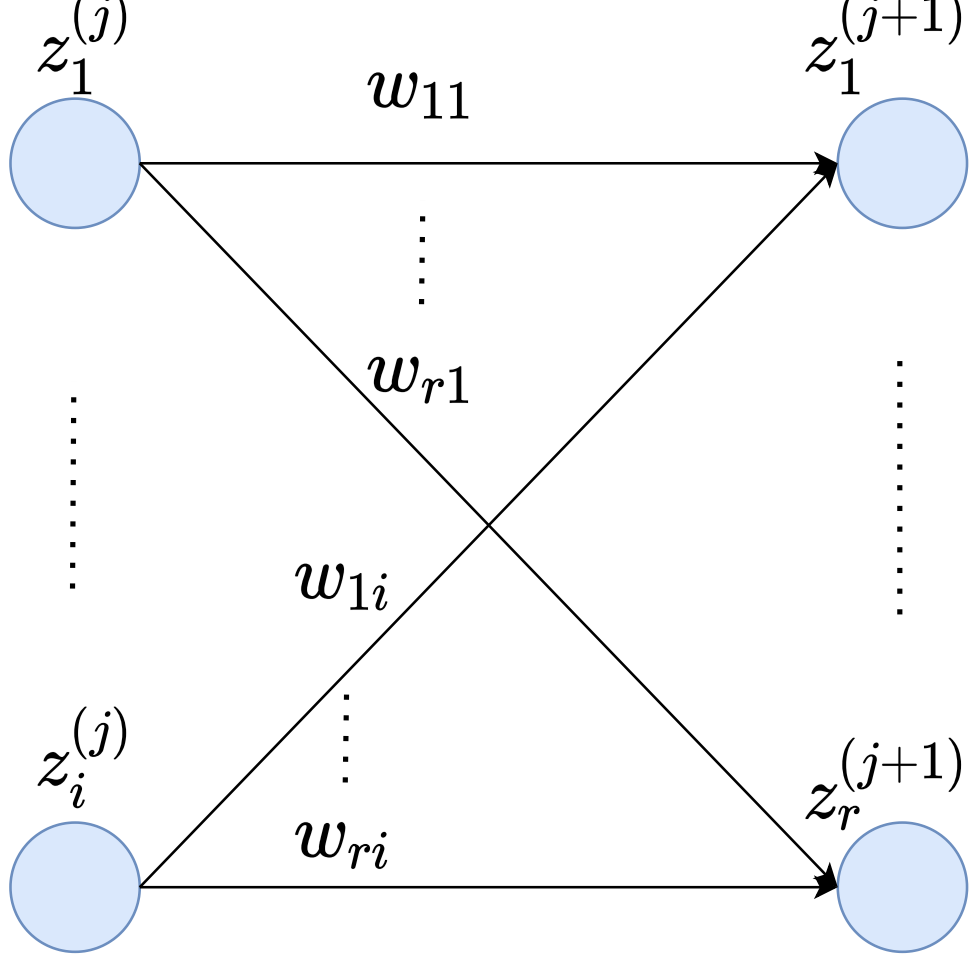


Figure 2: Enumerated weights according to their input and output nodes between layer j and $(j + 1)$

The weight matrix \mathbf{W}_{j+1} maps the weights from layer j to layer $j + 1$. \mathbf{W}_{j+1} is arranged as follows:

$$\mathbf{W}_{j+1} = \begin{bmatrix} w_{11} & w_{12} & \dots & w_{1i} \\ w_{21} & w_{22} & \dots & w_{2i} \\ \vdots & \ddots & & \\ w_{r1} & w_{r2} & \dots & w_{ri} \end{bmatrix}. \quad (25)$$

Regularization terms $R_{\ell_1, j+1}$ are defined for each weight matrix \mathbf{W}_{j+1} :

$$R_{\ell_1, j+1} = \sum_{i,k \in W_{j+1}} |w_{i,k}|. \quad (26)$$

where $w_{i,k}$ are the model weights from layer j to $j + 1$, or equivalently, the elements of \mathbf{W}_{j+1} . The regularization terms

for each layer are added to the cost function:

$$\mathbf{w}^* = \underset{\mathbf{w}}{\operatorname{argmin}} \left\{ \frac{1}{N} \sum_{i=1}^N (\mathbf{y}_i - \mathbf{f}(\mathbf{x}_i))^2 + \lambda_1 R_{\ell_1,1} \dots \right. \\ \left. + \lambda_{j+1} R_{\ell_1,j+1} + \dots + \lambda_L R_{\ell_1,L} \right\}, \quad (27)$$

where $\frac{1}{N} \sum_{i=1}^N (\mathbf{y}_i - \mathbf{f}(\mathbf{x}_i))^2$ is the MSE, and $\lambda_{j+1}, j = 0, \dots, 3$ is a layer-specific hyperparameter that determines how the weights in \mathbf{W}_{j+1} are penalized.

3.2. Experimental setup and data generation

Table 2: Constants in the simulator

Constant	Physical meaning	Numeric value
k_0	$1/(\rho_{sl} A_{sl})$	$2 \cdot 10^{-5}$
k_1	$2k_{sl} A_{sl} / \Delta_{fus} H_{cry}$	$7.5 \cdot 10^{-4}$
k_2	$h_{bath-sl} A_{sl} / \Delta_{fus} H_{cry}$	0.18
k_3	$0.002 \frac{M_{Al_2O_3} C^E}{z \cdot F}$	$1.7 \cdot 10^{-7}$
k_4	$C_{Na_2O} \frac{4M_{AlF_3}}{3M_{Na_2O}}$	0.036
k_5	$C_{Na_2O} \frac{2M_{cry}}{3M_{Na_2O}}$	0.03
k_6	$0.002 \frac{M_{Al} C^E}{z \cdot F}$	$4.43 \cdot 10^{-8}$
k_7	$k_2 \cdot c_{p_{cry, liq}}$	338
k_8	$k_1 \cdot c_{p_{cry, liq}}$	1.41
k_9	A_{sl}	17.92
k_{10}	$1/h_{bath-sl}$	0.00083
k_{11}	$1/(2k_{sl})$	0.2
k_{12}	$k_2 \cdot c_{p_{cry, s}}$	237.5
k_{13}	$k_1 \cdot c_{p_{cry, s}}$	0.99
k_{14}	$x_{wall} / (2k_{wall})$	0.0077
k_{15}	$1/(2k_{sl})$	0.2
k_{16}	T_0	35
k_{17}	$1/(m_{wall} c_{p, wall})$	$5.8 \cdot 10^{-7}$
k_{18}	$1/h_{wall-0}$	0.04
α	$1/c_{p_{bath, liq}}$	$5.66 \cdot 10^{-4}$
β	$1/c_{p_{cry, sol}}$	$7.58 \cdot 10^{-4}$

Data for the aluminium electrolysis process is generated by integrating the non-linear ODEs given by Eqs. (17) - (24) with a set of chosen initial values for the state variables $\mathbf{x}(t_0)$, and fourth-order Runge-Kutta (RK4) algorithm. The initial conditions of each variable x_i for each simulation are randomly chosen from a given interval of possible initial conditions:

Table 3 shows the intervals for initial conditions of each variable. For x_2 and x_3 , concentrations c_{x_2} and c_{x_3} are given.

Data-driven models depend on a high degree of variation in the training data to be reliable and valid in a large area of the input space. The input signal determines how the system is excited and thus what data is available for modeling and parameter estimation. Operational data from a controlled, stable process is generally characterized by a low degree of variation. Even large amounts of data sampled over a long period from a controlled process can not guarantee that the variation in the training data is large enough to ensure that the trained model generalizes to unseen data. Random excitations are added to the input signals to increase the variation in the sampled data. The intuition is that the random excitation will push the dynamics out of the standard operating condition so that variation in the training

Table 3: Initial conditions for system variables

Variable	Initial condition interval
x_1	[3260, 3260]
c_{x_2}	[0.02, 0.03]
c_{x_3}	[0.10, 0.12]
x_4	[13500, 14000]
x_5	[9950, 10000]
x_6	[975, 975]
x_7	[816, 816]
x_8	[580, 580]

data increases. In general, each control input i is given by:

$$u_i = \text{Deterministic term} + \text{Random term}. \quad (28)$$

The control inputs u_1 , u_3 and u_4 are impulses. The random term is zero for these control inputs when the deterministic term is zero. The deterministic term is a proportional controller. The control inputs u_2 and u_5 are always nonzero. These control inputs have constant deterministic terms and a random term that changes periodically. The random term stays constant for a certain period ΔT_{rand} before changing to a new randomly determined constant. Choosing the period ΔT_{rand} is a matter of balancing different objectives. On the one hand, it is desirable to choose a large period ΔT_{rand} so that the system can stabilize and evolve under the given conditions to reveal the system dynamics under the given conditions. On the other hand, it is desirable to test the systems under many different operational conditions. By empirically testing different periods ΔT_{rand} , and seeing how the dynamics evolve in simulation, it turns out that setting $\Delta T_{rand} = 30\Delta T$ is a fair compromise between the two. Table 4 gives the numerical values of the deterministic

Table 4: Control functions

Input	Deterministic term	Random term interval	ΔT_{rand}
u_1	$3e4(0.023 - c_{x_2})$	[-2.0, 2.0]	ΔT
u_2	$14e3$	[-7e3, 7e3]	$30 \cdot \Delta T$
u_3	$13e3(0.105 - c_{x_3})$	[-0.5, 0.5]	ΔT
u_4	$2(x_5 - 10e3)$	[-2.0, 2.0]	ΔT
u_5	0.05	[-0.015, 0.015]	$30 \cdot \Delta T$

term of the control input, the interval of values for the random terms, and the duration ΔT_{rand} of how long the random term is constant before either becoming zero (u_1, u_3, u_4) or changing to a new randomly chosen value (u_2, u_5). One simulation i with a given set of initial conditions is simulated for 1000 time steps, and each time step $\Delta T = 30s$. The simulation generate the data matrix as in Eq. (29):

$$\mathbf{X} = \begin{bmatrix} x_1(0) & x_2(0) & \dots & x_8(0) & u_1(0) & \dots & u_5(0) \\ x_1(1) & x_2(1) & \dots & x_8(1) & u_1(1) & \dots & u_5(1) \\ \vdots & \vdots & \ddots & \vdots & \vdots & \ddots & \vdots \\ x_1(k) & \dots & x_1(k) & \dots & u_1(k) & \dots & u_5(k) \\ \vdots & \vdots & \ddots & \vdots & \vdots & \ddots & \vdots \\ x_1(999) & x_2(999) & \dots & x_8(999) & u_1(999) & \dots & u_5(999) \end{bmatrix}. \quad (29)$$

The number k within the parenthesis of variable i indicate the time step for when $x_i(k)$ is sampled. The target values

are then calculated as

$$\mathbf{Y} = \begin{bmatrix} \frac{x_1(1)-x_1(0)}{\Delta T} & \dots & \frac{x_8(1)-x_8(0)}{\Delta T} \\ \frac{x_1(2)-x_1(1)}{\Delta T} & \dots & \frac{x_8(2)-x_8(1)}{\Delta T} \\ \vdots & \ddots & \vdots \\ \frac{x_1(k)-x_1(k-1)}{\Delta T} & \dots & \frac{x_8(k)-x_8(k-1)}{\Delta T} \\ \vdots & \ddots & \vdots \\ \frac{x_1(999)-x_1(998)}{\Delta T} & \dots & \frac{x_8(999)-x_8(998)}{\Delta T} \end{bmatrix}. \quad (30)$$

The training set consist of smaller training sets \mathcal{S}_k :

$$\mathcal{S}_{train} = \{\mathcal{S}_1, \mathcal{S}_2, \dots, \mathcal{S}_k, \dots, \mathcal{S}_n\}. \quad (31)$$

Here, n is the number of simulated time-series \mathbf{X} . Each training set \mathcal{S}_k from simulation k are put in pairs for regression:

$$\mathcal{S}_k = [\mathbf{X}, \mathbf{Y}] = \begin{bmatrix} [\mathbf{x}(1), \mathbf{u}(1)], & \mathbf{y}(1) \\ \vdots & \vdots \\ [\mathbf{x}(k), \mathbf{u}(k)], & \mathbf{y}(k) \\ \vdots & \vdots \\ [\mathbf{x}(999), \mathbf{u}(999)], & \mathbf{y}(999) \end{bmatrix}. \quad (32)$$

The number of time series simulations n varies in the experiments to evaluate the model performance as a function of training size. The test set also consists of several time series simulations generated in the same way described above. The test set is given by:

$$\mathcal{S}_{test} = \{\{X_1\}, \{X_2\}, \dots, \{X_p\}\}. \quad (33)$$

$\mathcal{S}_{test}(i) = \{X_i\} = \{(\mathbf{x}_k, \mathbf{u}_k)\}_{k=1}^{1000}$ is one simulated time series, and $\{\mathbf{x}_k\}_{k=1}^{1000}$ is being forecasted by the models. $p = 20$ is the number of simulated time series in the test set. In all experiments 20 models of each dense and sparse networks with different initialization are trained on a training set and evaluated on a test set.

3.3. Performance metrics

In aluminum electrolysis, data is generally sampled at rare instants during the operation. Thus, a model needs to accurately forecast several time steps without feedback from measurements to ensure safe and optimal operation. Therefore, the models' capability to estimate the states \mathbf{x} over a given time horizon without measurement feedback becomes an important measure of performance. The initial conditions $\mathbf{x}(t_0)$ are given to the models. Then the consecutive n time steps of the states are estimated $\{\hat{\mathbf{x}}(t_1), \dots, \hat{\mathbf{x}}(t_n)\}$. This is called a **rolling forecast**. The model estimates the time derivatives of the states $d\hat{\mathbf{x}}_i/dt$ based on the current control inputs $\mathbf{u}(t_i)$ and initial conditions $\mathbf{x}_0(t)$ if $t = t_0$, or the estimate of the current state variables $\hat{\mathbf{x}}(t_i)$ if $t > t_0$:

$$\frac{d\hat{\mathbf{x}}(t_i)}{dt} = \begin{cases} \hat{f}(\hat{\mathbf{x}}(t_i), \mathbf{u}(t_i)), & \text{if } t_i > t_0 \\ \hat{f}(\mathbf{x}_0(t_i), \mathbf{u}(t_i)), & \text{if } t_i = t_0 \end{cases} \quad (34)$$

Then, the next state estimate $\mathbf{x}(t_{i+1})$ is calculated as

$$\hat{\mathbf{x}}(t_{i+1}) = \hat{\mathbf{x}}(t_i) + \frac{d\hat{\mathbf{x}}(t_i)}{dt} \cdot \Delta T. \quad (35)$$

The rolling forecast can be computed for each of the states x_i for one set of test trajectories \mathcal{S}_{test} . However, presenting the rolling forecast of multiple test sets would render the interpretation difficult. By introducing a measure called Average Normalized Rolling Forecast Mean Squared Error (AN-RFMSE) that compresses the information about

model performance, the models can easily be evaluated on a large number of test sets. The AN-RFMSE is a scalar defined as:

$$\text{AN-RFMSE} = \frac{1}{p} \sum_{i=1}^p \frac{1}{n} \sum_{j=1}^n \left(\frac{\hat{x}_i(t_j) - x_i(t_j)}{\text{std}(x_i)} \right)^2, \quad (36)$$

where $\hat{x}_i(t_j)$ is the model estimate of the simulated state variable x_i at time step t_j , $\text{std}(x_i)$ is the standard deviation of variable x_i in the training set \mathcal{S}_{train} , $p = 8$ is the number of state variables and n is the number of time steps the normalized rolling forecast MSE is averaged over. Hence, for every model \hat{f}_j and every test set time series $\mathcal{S}_{test}(i)$, there is a corresponding AN-RFMSE. This generates a matrix, where each row represents individual model instances, and every column represents one test set simulation $\mathcal{S}_{test}(i)$. Each entry in the matrix is the AN-RFMSE for a given model instance and a given $\mathcal{S}_{test}(i)$. The matrix is given by:

$$\text{AN-RFMSE}_{mat} = \begin{bmatrix} \text{AN-RFMSE}_{11} & \dots & \text{AN-RFMSE}_{1n} \\ \vdots & \vdots & \vdots \\ \text{AN-RFMSE}_{k1} & \dots & \text{AN-RFMSE}_{kn} \end{bmatrix}. \quad (37)$$

k is the number of models, and n is the number of time series simulations in the test set \mathcal{S}_{test} . There are two AN-RFMSE_{mat} matrices, one for sparse models and one for dense models. Averaging over all columns at each row, that is, averaging over all test set time series for each model instance, generates a vector

$$\overline{\text{AN-RFMSE}}_{vec} = \begin{bmatrix} \frac{1}{n} \sum_{i=1}^n \text{AN-RFMSE}_{1i} \\ \vdots \\ \frac{1}{n} \sum_{i=1}^n \text{AN-RFMSE}_{ki} \end{bmatrix} = \begin{bmatrix} \overline{\text{AN-RFMSE}_1} \\ \vdots \\ \overline{\text{AN-RFMSE}_k} \end{bmatrix}. \quad (38)$$

The elements of $\overline{\text{AN-RFMSE}}_{vec}$ is the average AN-RFMSE over all test set time series for every model instance.

4. Results and discussion

In this section, we present and discuss the main findings of the work. In doing so, we will analyze the results from the perspective of interpretability, generalizability and training stability.

4.1. Interpretability perspective

As discussed earlier, the interpretability of a model is the key to its acceptability in high-stake applications like the aluminum extraction process considered here. Unfortunately, highly complex dense neural networks having thousands to millions of parameters which were the starting point for the modeling here are almost impossible to interpret. Refer to the Fig. 3 that shows the model structure of a dense DNN model learned for the generated data.

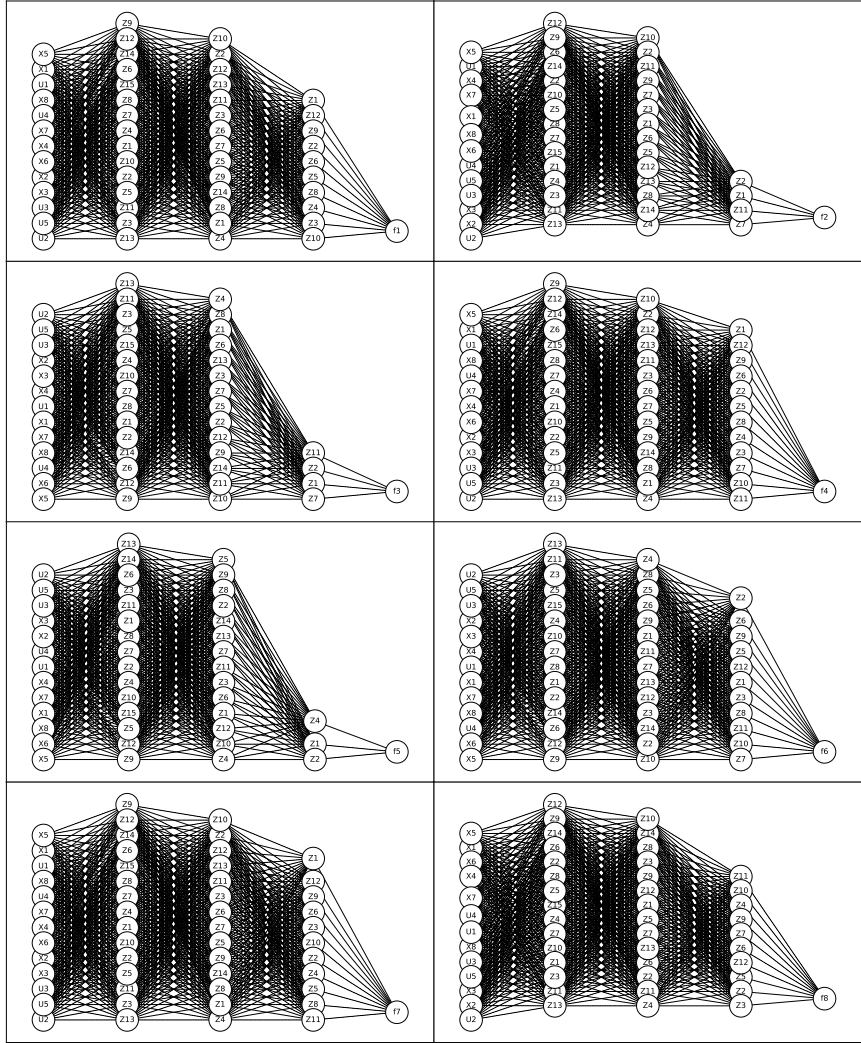


Figure 3: Model structure of each output function $\{f_1, \dots, f_8\}$ for one of the trained dense neural network models. Blue circles represent neurons, inputs and outputs in the model. X_i represent system variable i in the input layer, U_i represents control input i in the input layer, and Z_i represents latent variable i in the layer it is visualized. The directed edges indicate weights in the model.

Fortunately, through the regularization it was possible to significantly reduce the model complexity resulting in a drastically reduced number of trainable parameters (see the Figs. 4-11). It can be argued that the reduced model complexity of sparse neural networks increases the model interpretability. With domain knowledge about the aluminum electrolysis process, the sparse models can be evaluated as we will do in the remainder of this section.

The results related to the interpretability aspect is presented in the form of model structure plots which can be used to explain the input-output mapping of the models. If the model structures are very sensitive to the initialization, then there interpretation will not make sense therefore, 100 DNNs with different initialization are trained independently and their common trends are emphasized in the discussions. We now present each of the model outputs $\{\hat{f}_1(\mathbf{x}, \mathbf{u}), \dots, \hat{f}_8(\mathbf{x}, \mathbf{u})\}$. It is worth mentioning that these outputs are estimates of each of the time derivatives of the states $\{\dot{x}_1, \dots, \dot{x}_8\}$ respectively.

4.1.1. Model output \hat{f}_1

The simulation model for the first output f_1 defined in Eq. (17) is a function of the features $\{x_1, x_2, x_3, x_4, x_6, x_7\}$. f_1 can further be divided into three sums $f_1 = h_1(x_1, x_2, x_3, x_4, x_7) + h_2(x_6) + h_3(x_2, x_3, x_4)$, where $h_1 = k_1 \frac{g_1(x_2, x_3, x_4) - x_7}{k_0 x_1}$,

Table 5: Frequency of learned features for each output $\{\hat{f}_1, \dots, \hat{f}_8\}$. Each column i correspond to an output \hat{f}_i of the neural network. Each row element j correspond to one of the features $\{x_1, x_2, \dots, x_8, u_1, u_2, \dots, u_5\}$. The value of the table element (i, j) is the percent of how many out of one hundred models of the output \hat{f}_i that feature j occurs.

Feature	Output functions							
	\hat{f}_1	\hat{f}_2	\hat{f}_3	\hat{f}_4	\hat{f}_5	\hat{f}_6	\hat{f}_7	\hat{f}_8
x_1	86	1	1	86	2	100	99	100
x_2	100	2	2	100	1	100	100	100
x_3	100	2	2	100	0	93	100	87
x_4	100	0	0	100	0	87	100	87
x_5	2	0	0	2	0	2	2	2
x_6	100	2	2	100	1	100	100	87
x_7	22	1	1	21	1	7	89	89
x_8	100	1	1	100	2	87	100	100
u_1	100	100	100	100	0	100	100	87
u_2	4	0	0	4	1	100	18	18
u_3	2	0	100	2	0	2	4	4
u_4	2	0	0	2	100	3	3	3
u_5	3	0	0	3	1	100	18	18

$h_2 = -k_2 x_6$ and $h_3 = g_1(x_2, x_3, x_4)$. g_1 is a nonlinear function defined in Eq. (11).

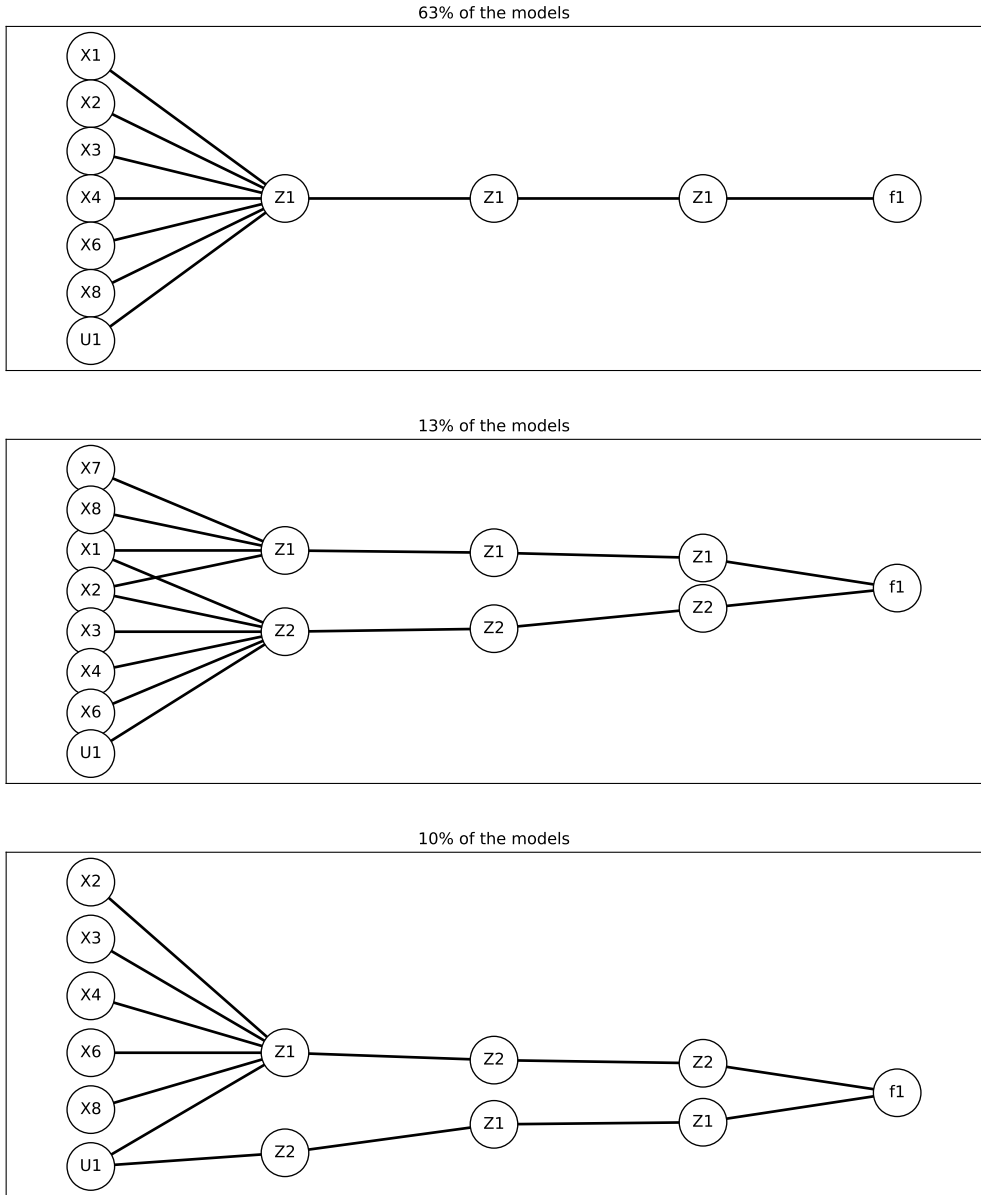


Figure 4: Most common learned structures for $\hat{f}_1(\mathbf{x}, \mathbf{u})$.

Fig. 4 shows the three most common learned structures of the first output of the neural network $\hat{f}_1(\mathbf{x}, \mathbf{u})$. In total, these structures account for 86% of all learned structures of \hat{f}_1 . The top structure forms the resulting structure for 63% of the models. It is a function of seven inputs $\hat{f}_1 = f(x_1, x_2, x_3, x_4, x_6, x_8, u_1)$. All input features are connected to the same neuron in the first layer. Moreover, it is only one neuron in each hidden layer. The upper bound in Eq. (9) states that this model structure only has $n^{dL} = 1^{7-3} = 1$ region. This is equivalent to stating that the model collapses to one linear model. The middle and the bottom structures of Fig. 4 have more than one neuron in the hidden layers. However, the structures can be divided into two disconnected subnetworks since the hidden neurons are not connected before they are added in the output layer. Hence, also these models collapse to linear models with a single region. This means that the neural networks do not capture the nonlinear dynamics in the simulation model. All structures of Fig. 4 are erroneously including x_8 and u_1 in their feature basis. Besides, x_7 which is present in the simulation model f_1 is

not found by the top and bottom structures in Fig. 4. In fact, x_7 is found only in 22% of the models \hat{f}_1 according to Table 5. The exact cause of this erroneous feature selection is not trivial. However, x_8 which is the wall temperature correlates highly with the side ledge temperature x_7 . Thus, x_8 can possibly have been learned as a feature of f_1 instead of x_7 . Moreover, the alumina feed u_1 on the other hand affects the time derivative of the mass of alumina \dot{x}_2 , the time derivative of mass of aluminum fluoride \dot{x}_3 and the time derivative of cryolite \dot{x}_4 directly. All these variables affect \dot{x}_1 through the liquidus temperature $g_1(x_2, x_3, x_4)$. To understand how this might cause the learning algorithm to find u_1 as a feature of \hat{f}_1 , consider the following: let u_1 be zero until time t . Then, $\{x_2, x_3, x_4\}$ will be updated due to u_1 at the next sampled time step $t + 1$. However, the fourth-order Runge Kutta solver splits the sampling interval into 4 smaller intervals $\{t + 0.25, t + 0.5, t + 0.75, t + 1\}$ and solve the ODE equations at all these time steps. Thus, the state variables $\{x_2, x_3, x_4\}$ are updated already at time $t + 0.25$. Since \dot{x}_1 is depending on these variables, x_1 will be updated at $t + 0.5$. Therefore, at time $t + 1$, when data is sampled, x_1 would also be changed. Hence, the learning algorithm finds u_1 to affect the time derivative \dot{x}_1 . This could have been solved by shortening the sampling interval. Furthermore, x_1 is not included as a feature in 14% of the models. This might be a combination of parameter initialization and that x_1 is multiplied by the small constant $k_0 = 2 \cdot 10^{-5}$.

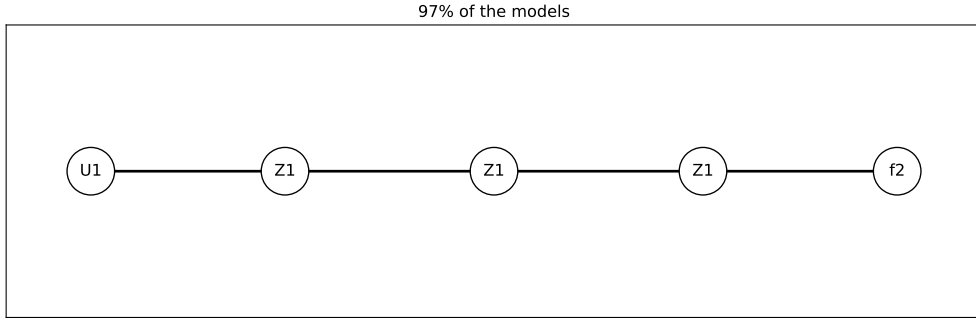


Figure 5: Most common learned structure for $\hat{f}_2(\mathbf{x}, \mathbf{u})$. 97% of f_2 ends up with this structure.

4.1.2. Model output \hat{f}_2

Fig. 5 shows the most common learned structure among the models \hat{f}_2 that models the time derivative of alumina $f_2 = \dot{x}_2$. 97% of the structures end up as the structure in Fig. 5. The simulation model f_2 in Eq. (18) is a linear model dependent on $\{u_1, u_2\}$. The learned models \hat{f}_2 only finds u_1 as the relevant feature. The reason for this might be that u_2 is proportional to a very small constant $k_3 = 1.7 \cdot 10^{-7}$. Variations in the line current u_2 are not big enough to be of significance for the learning algorithm. The dynamics caused by u_2 is instead captured in a bias in the models.

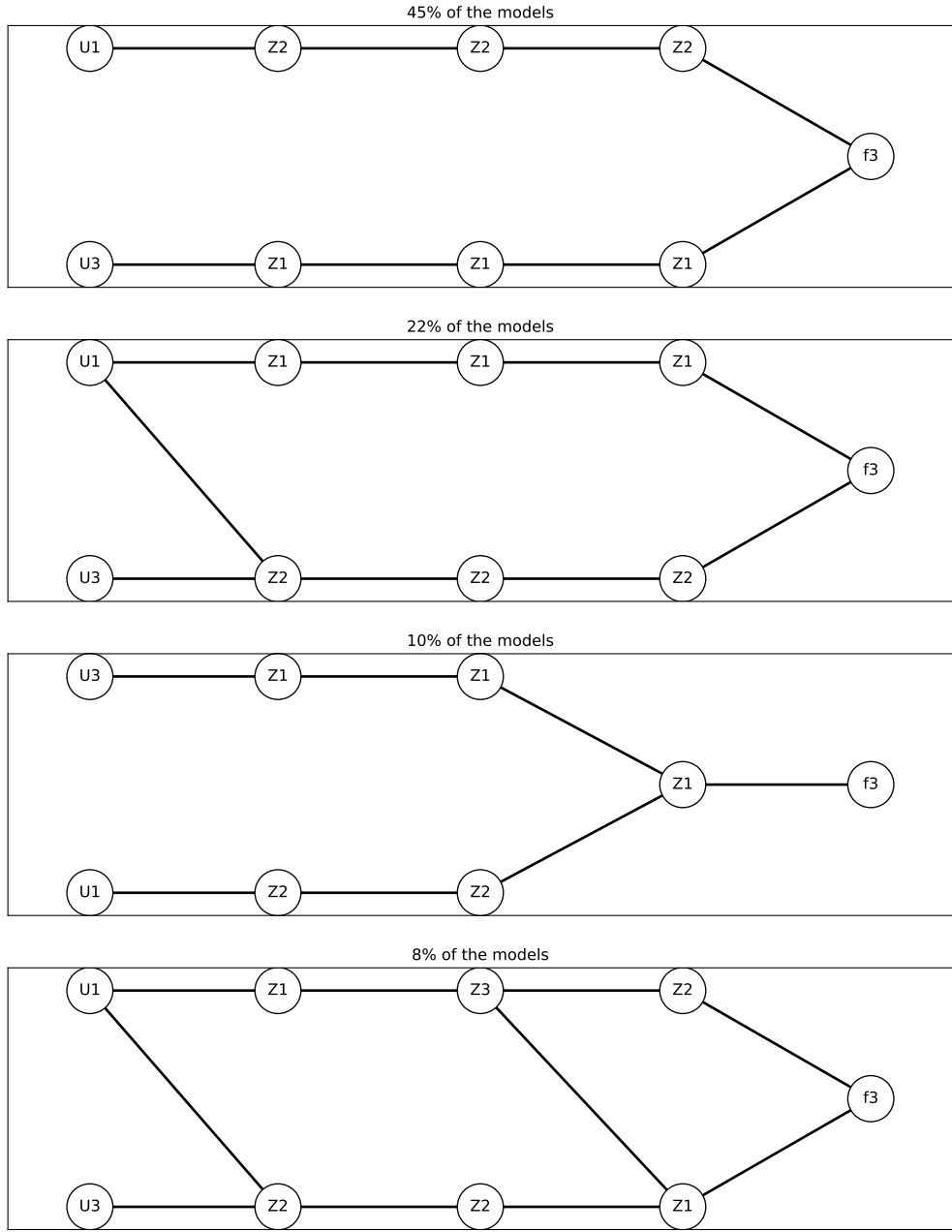


Figure 6: Most common learned structures for $\hat{f}_3(\mathbf{x}, \mathbf{u})$.

4.1.3. Model output \hat{f}_3

Fig. 6 shows the four most common learned structures of \hat{f}_3 . \hat{f}_3 models the time derivative of the aluminum fluoride mass \dot{x}_3 in the cell. The simulation model $\dot{x}_3 = f_3$ in Eq. (19) is a linear model depending on the features $\{u_1, u_3\}$, and in all structures in Fig. 6, only these two features are found. As shown in Table 5, these features are found in 100% of the trained models. The structures found are mainly linear models, however in the second and forth structures, there are some weights that connects the features in intermediate layers.

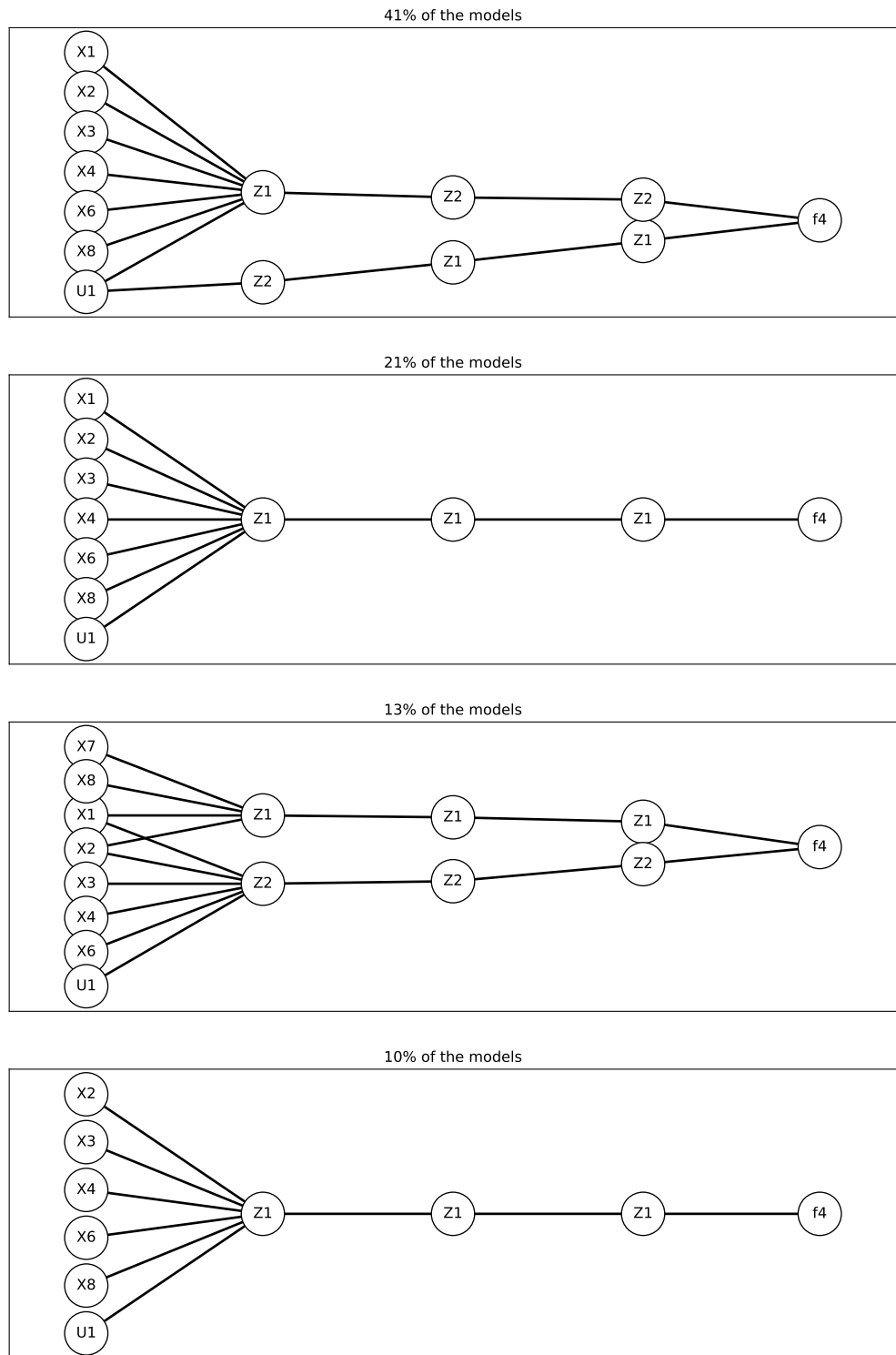


Figure 7: Most common learned structures for $\hat{f}_4(\mathbf{x}, \mathbf{u})$.

4.1.4. Model output \hat{f}_4

Fig. 7 show the four most common learned structures among models \hat{f}_4 that models the mass rate of liquid cryolite Na_3AlF_6 in the bath, namely \dot{x}_4 . \dot{x}_4 is simulated by the simulation model $\dot{x}_4 = f_4$ in Eq. (19). f_4 consist of the features $\{x_1, x_2, x_3, x_4, x_6, x_7, u_1\}$. Table 5 show that $\{x_2, x_3, x_4, x_6, x_8, u_1\}$ are included in 100% of the learned models, x_1 is included in 86% of the models and x_7 is included in only 21% of the models. As for \hat{f}_1 , x_8 is erroneously included in the basis of the model. This might be explained by that x_7 and x_8 highly correlates, and that the wrong feature is included. The structures in Fig. 7 are all forming linear models. However, the simulation model $\dot{x}_4 = f_4$ is partly nonlinear. Thus, the approximation \hat{f}_4 oversimplifies the dynamics. This might be caused by a high weighting of the sparse regularisation term. If the loss function is less penalized, it is room for more weights in the model and therefore also more nonlinearities.

4.1.5. Model output \hat{f}_5

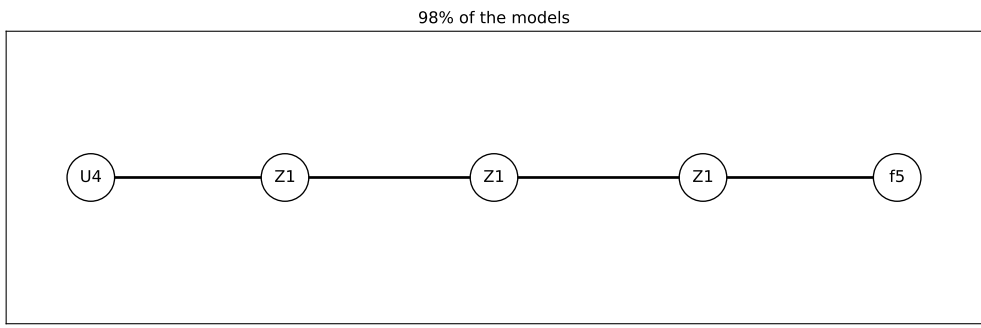


Figure 8: Most common learned structures for $\hat{f}_5(\mathbf{x}, \mathbf{u})$.

Fig. 8 show the most common learned structure among the models \hat{f}_5 and include 98% of the learned model structures. \hat{f}_5 is modeling the mass rate of produced aluminum in the cell \dot{x}_5 . The x_5 time series are produced by the simulation model $\dot{x}_5 = f_5$ in Eq. 21. f_5 is a linear model dependent on the features $\{u_2, u_4\}$. However, most of the model structures are only depending on u_4 . This can be caused by the fact that u_2 is proportional to a very small constant $k_6 = 4.43 \cdot 10^{-8}$. Thus, variations in u_2 might not be large enough for the learning algorithm to find u_2 significant as a basis for \hat{f}_5 .

4.1.6. Model output \hat{f}_6

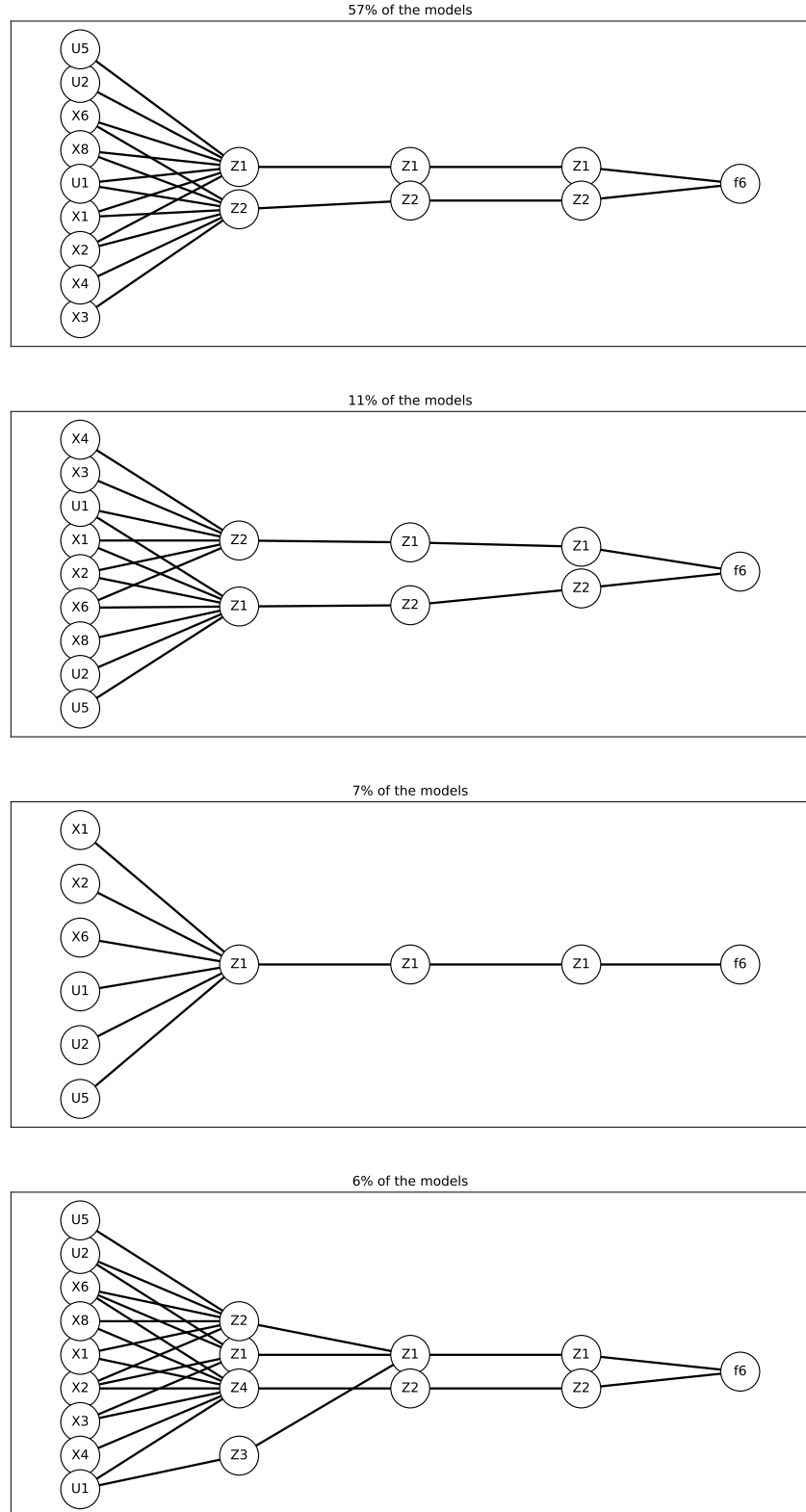


Figure 9: Most common learned structures for $\hat{f}_6(\mathbf{x}, \mathbf{u})$.
21

Fig. 9 show the most common model structures of \hat{f}_6 . \hat{f}_6 models the bath temperature time derivative \dot{x}_6 . The bath temperature x_6 is simulated by the ODE in Eq. (22). It is a nonlinear equation depending on $\{x_1, x_2, x_3, x_4, x_6, x_7, u_2, u_5\}$. The most common structure, learned by 57% of the models \hat{f}_6 is illustrated in the top plot of Fig. 9. This structure has the basis $\{x_1, x_2, x_3, x_4, x_6, x_8, u_1, u_2, u_5\}$. Hence, it finds u_1 and x_8 , which is erroneously found in many of the structures above. A possible explanation for this trend is given above. The structure has two neurons in the first layer, one with the basis $\{x_1, x_2, x_6, x_8, u_1, u_2, u_5\}$ and one with the basis $\{x_1, x_2, x_3, x_4, x_6, x_8, u_1\}$. Since the model collapses to a linear model, all terms are summed in the end. Thus, the separation of the basis is thus of little importance. The second plot from above in Fig. 9 is the second most common structure, and accounts for 11% of the models \hat{f}_6 . It has the same feature basis as the most common structure, but they are arranged differently in the first layer. However, since both model structures are linear models, this arrangement is of minor importance. The third structure in Fig. 9 which account for 7% of the structures of \hat{f}_6 has the basis $\{x_1, x_2, x_6, u_1, u_2, u_5\}$. Compared to the other structures, $\{x_3, x_4, x_8\}$ is not present. Since it only happens rarely, this is maybe partly caused by bad parameter initialization. The fourth most common structure, which accounts for 6% of the structures, has the same feature basis as the first and the second most common structures. This structure is plotted in the bottom of Fig. 9. While all other structures in Fig. 9 have one linear response region, the fourth most common model structure models some nonlinearities. That is, neurons in the first hidden layer are connected in the second hidden layer. Hence, the input space must be divided into several linear response regions for this structure.

4.1.7. Model output \hat{f}_7

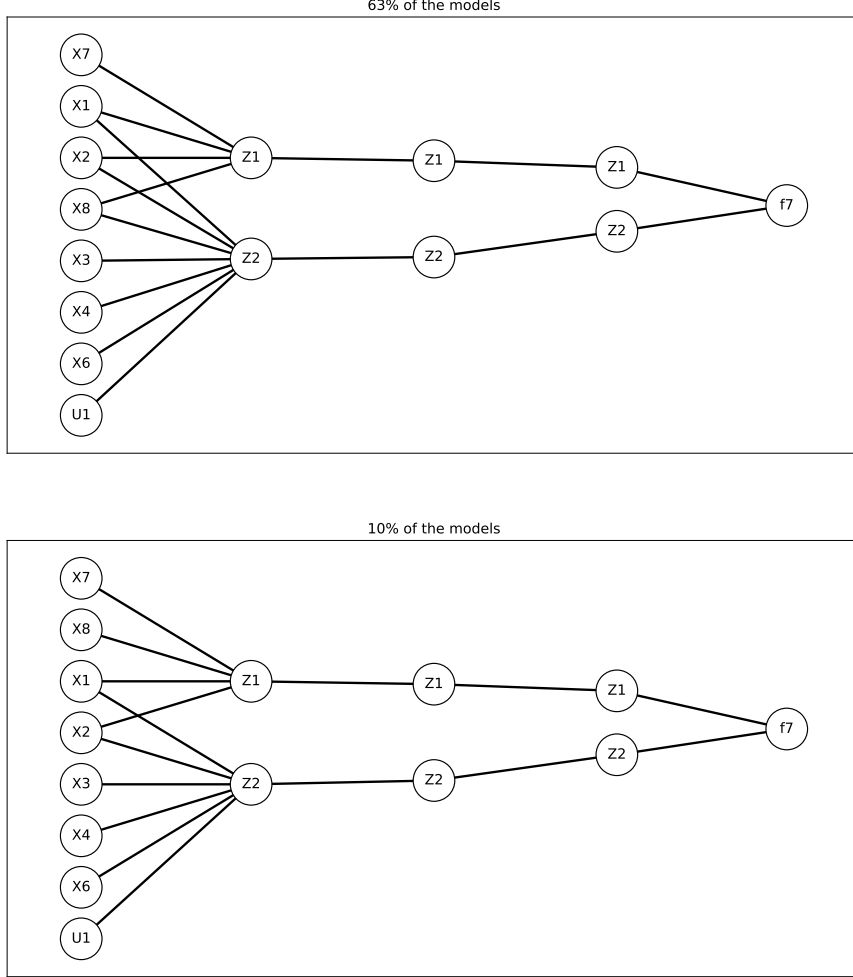


Figure 10: Most common learned structures for $\hat{f}_7(\mathbf{x}, \mathbf{u})$.

Fig. 10 show the two most common structures for the models \hat{f}_7 . \hat{f}_7 models the time derivative of the side ledge temperature \dot{x}_7 . $\dot{x}_7 = f_7$ is simulated by the ODE in Eq. (23). \dot{x}_7 is depending on the feature basis $\{x_1, x_2, x_3, x_4, x_6, x_7, x_8\}$. Table 5 states that the basis $\{x_2, x_3, x_4, x_6, x_8, u_1\}$ is present for 100% of the models, x_1 is present for 99% of the models and x_7 is present in 89% of the models. The top plot in Fig. 10 show the structure that accounts for 63% of the models. The bottom plot account for 10% of the model structures of \hat{f}_7 . These two structures collapse to linear models, and have the same feature basis $\{x_1, x_2, x_3, x_4, x_6, x_7, x_8, u_1\}$, but have minor differences in how weights are connected between input layer and first hidden layer. u_1 is also for this model output erroneously found as a basis, and a possible explanation is mentioned above.

4.1.8. Model output \hat{f}_8

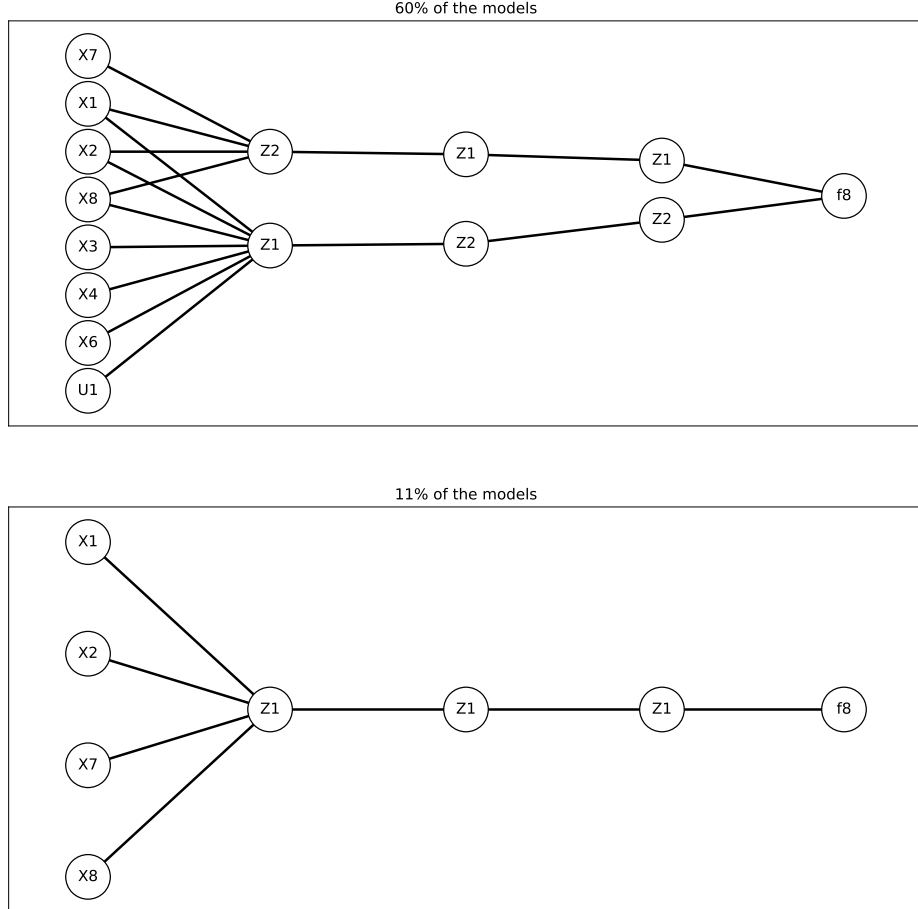


Figure 11: Most common learned structures for $\hat{f}_8(\mathbf{x}, \mathbf{u})$.

Fig. 11 show the two most common model structures for the last model output \hat{f}_8 . \hat{f}_8 models the time derivative of the wall temperature $\dot{x}_8 = f_8$, which is simulated in Eq. (24). \dot{x}_8 depends on the feature basis $\{x_1, x_7, x_8\}$. However, the most common learned structure for \hat{f}_8 has the basis $\{x_1, x_2, x_3, x_4, x_6, x_7, x_8, u_1\}$. This is the exact same structure as the most common learned structure for \hat{f}_7 . Therefore, a possible explanation is that \hat{f}_8 adapts the same parameters as \hat{f}_7 in some cases as they highly correlates. The bottom plot in Fig. 11 show the second most common learned structure of the model output \hat{f}_8 . This structure is learned by 11% of the models \hat{f}_8 . The feature basis for this structure is $\{x_1, x_2, x_7, x_8\}$, and reminds more of the actual basis. In this structure, there is only one erroneous learned feature, namely x_2 . Fig. 4-11 and Table 5 show that the sparse learning is quite consistent in finding the same feature basis and structure with similar characteristics. However, some differences that affect the models are present.

It is clear that doing a similar analysis for models in Fig. 3 is impossible as all interconnections make the models a black box. On average, 93% of the weights in the sparse DNN models are pruned. For the outputs $\hat{f}_1, \hat{f}_4, \hat{f}_6, \hat{f}_7$ and \hat{f}_8 , approximately 40% of the input features are pruned of the model structures. For \hat{f}_2, \hat{f}_3 and \hat{f}_5 , 85 – 95% of the input features are pruned. For all outputs of the sparse DNN models, around 85 – 95% of the neurons are pruned at each layer. In a neural network, the number of matrix operations only decreases if neurons are pruned. That is, removing a neuron in layer j is equivalent to removing a row in weight matrix \mathbf{W}_j and a column in weight matrix \mathbf{W}_{j+1} . The dense models have a compact model structure, where most of the weights are nonzero. The dense DNN models in the case study have the shapes 13-15-14-12-8. The first number is the number of features, the second, third,

and fourth numbers are the numbers of neurons in hidden layers, and the last number is the number of outputs. This shape gives 669 matrix operations in a forward pass. An average sparse DNN, has the shape 13 – 6 – 6 – 6 – 8. This gives 198 matrix operations. Thus, the number of matrix operations in the forward pass of a sparse DNN model is reduced by approximately 70%.

4.2. Generalizability perspective

This section focuses on the models' performance on test data in terms of accuracy and uncertainty. Furthermore, we also investigate the impact of the training data quantity and prediction horizon on the performance measured in terms of AN-RFMSE.

4.2.1. Comparison of sparse and dense rolling forecast

Fig. 12 and Fig. 13 show the performance of 20 sparse and 20 dense DNN models with different parameter initialization forecasting the state variables \mathbf{x} in one of the time series in the test set $\mathcal{S}_{test}(i) = \{\mathbf{X}_i\}$ as defined in Eq. (33). The models are trained on a data set $\mathcal{S}_{train} = \{\{\mathbf{X}_1, \mathbf{Y}_1\}, \{\mathbf{X}_2, \mathbf{Y}_2\}, \dots, \{\mathbf{X}_{10}, \mathbf{Y}_{10}\}\}$ consisting of ten time series $\{\mathbf{X}_1, \dots, \mathbf{X}_{10}\}$ with 999 time steps each.

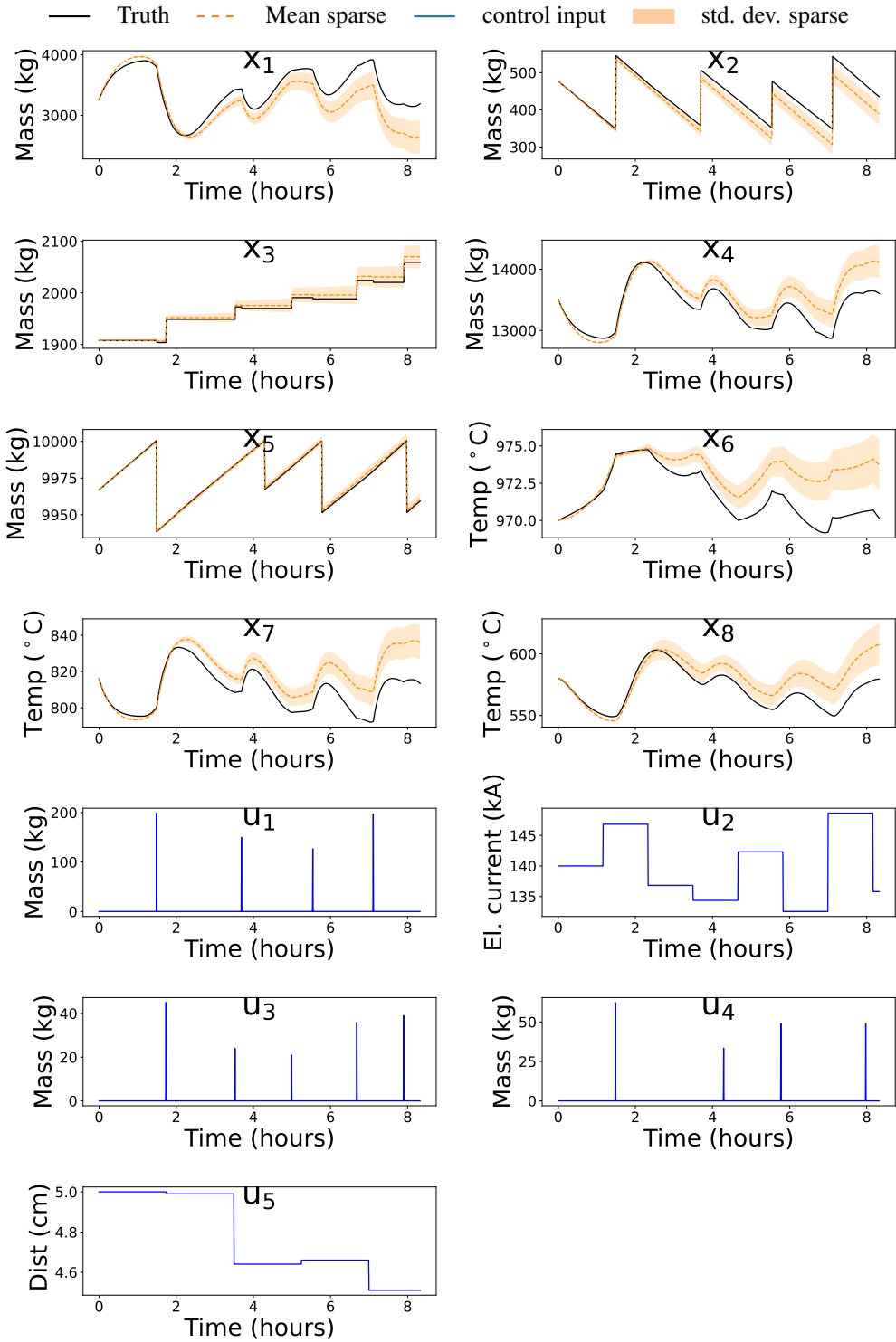


Figure 12: Sparse rolling forecast of state variables $\{x_1, \dots, x_8\}$ at each time instant. The true values of \mathbf{x} and control inputs \mathbf{u} are taken from one simulated set of test set trajectories $\mathbf{X}_i \in \mathbf{X}_{test}$. The orange dotted line shows the average of 20 forecasts calculated by 20 sparse neural network models with different parameter initialization. The orange band shows the standard deviation of the same 20 forecasts calculated by 20 sparse models.

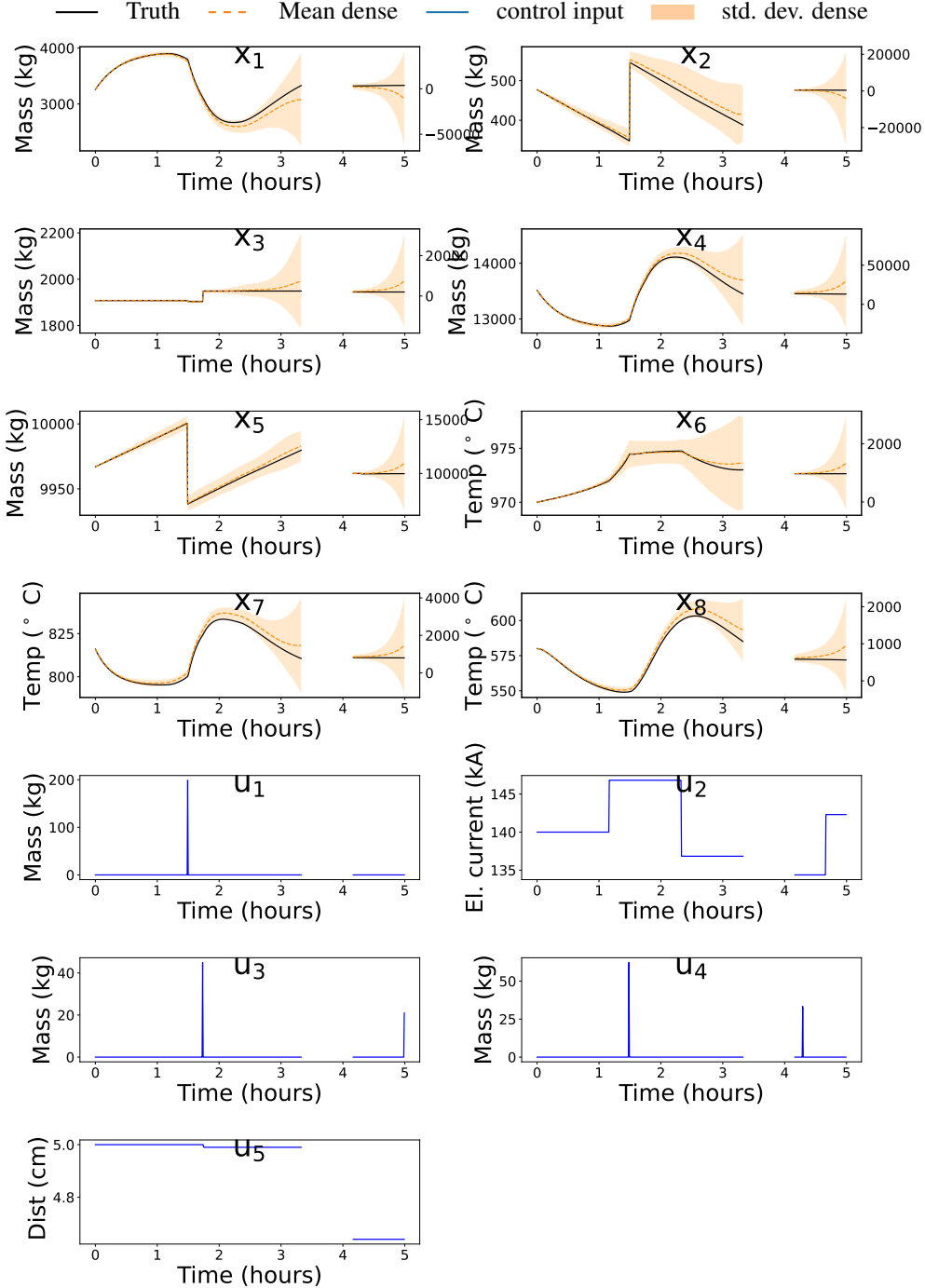


Figure 13: Dense rolling forecast of state variables $\{x_1, \dots, x_8\}$ at each time instant. The true values of \mathbf{x} and control inputs \mathbf{u} are taken from one simulated set of test set trajectories $\mathbf{X}_i \in \mathbf{X}_{test}$. The orange dashed line shows the average of 20 forecasts calculated by 20 dense neural network models with different parameter initialization. The orange band shows the standard deviation of the same 20 forecasts calculated by 20 dense models. The plots are divided into two regions on the x-axis with two different scales on the y-axis. The first region from time step zero until approximately time step 400 has the y-scale on the left side of the plots. The second region, from time step 500 to time step 700, has the y-scale on the right side of the plots. The first region shows the average and the standard deviation before the average forecast standard deviation drifts exponentially from the true values. The second region shows the exponential drift of the mean and standard deviation of the forecasts.

Fig. 12 and Fig. 13 indicate that the forecasts of sparse and dense models are showing similar performance for the first time steps after they are given the initial conditions. However, while the forecasts calculated by sparse models show a consistently slow drift from the simulated values of \mathbf{x} , the mean and standard deviation of forecasts calculated by dense models suddenly drifts exponentially. The narrow banded standard deviation of sparse neural networks can indicate that these models converge to models with similar characteristics during training despite different parameter initialization. Furthermore, the consistently slow drift between the sparse DNN model forecast of \mathbf{x} and the true values of \mathbf{x} indicate that the sparse models are generalizing better as they are showing good forecasting capabilities in a broader region than the dense DNN models. Fig. 12 and Fig. 13 show some interesting results that indicate better generalization of sparse DNN models than dense DNN models and that the convergence of model parameters for sparse DNN models are more robust to random initialization than dense DNN models are.

4.2.2. Impact of the training data quantity and prediction horizon

Fig. 14 shows the median, maximum and minimum elements of the $\overline{\text{AN-RFMSE}}_{vec}$ vector.

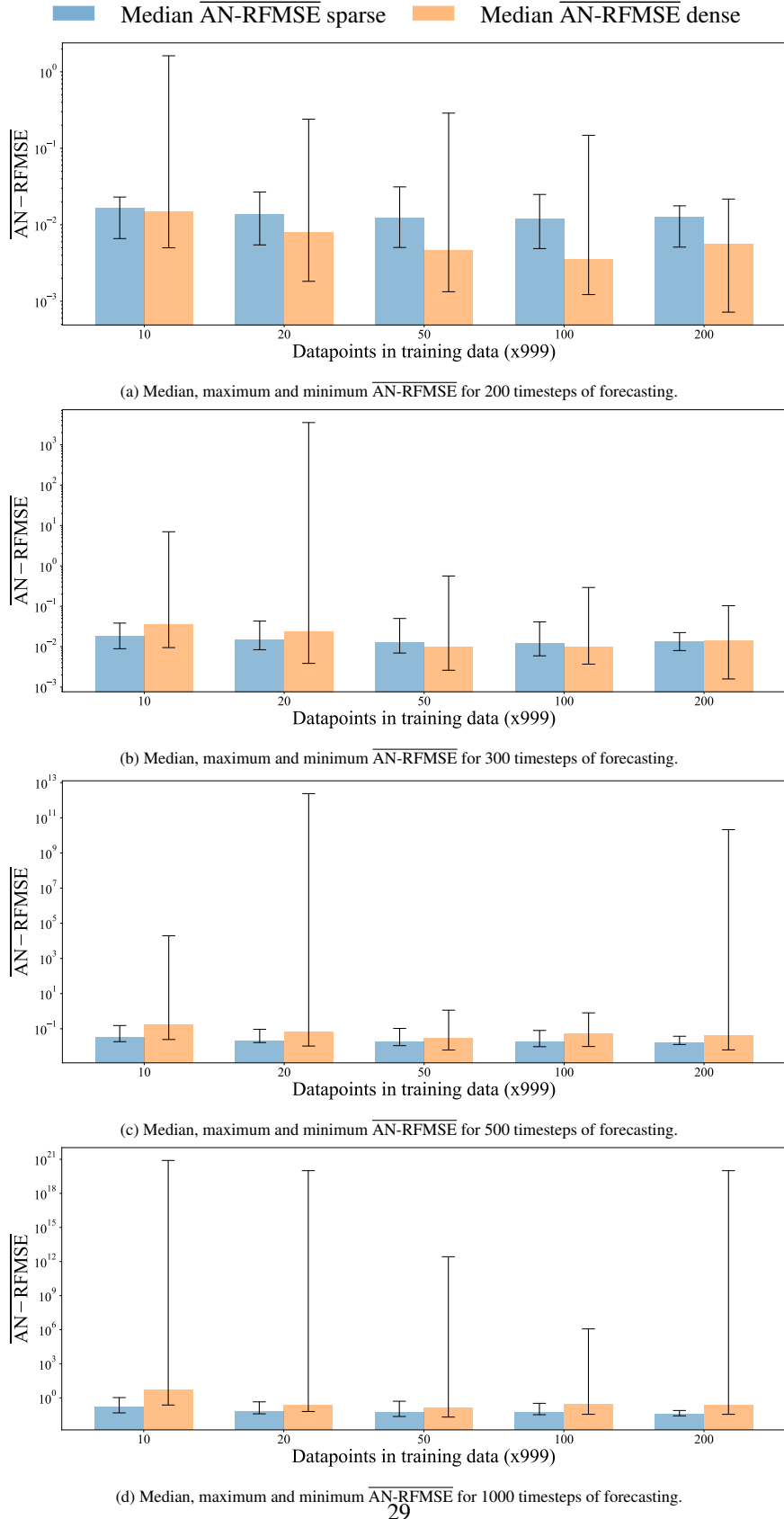


Figure 14: Median, maximum and minimum $\overline{\text{AN-RFMSE}}$. There are five groups of models of both sparse and dense DNNs trained on data sets with different sizes. For each group of models, there is a corresponding colored bar indicating median values and an error bar indicating maximum and minimum values of the vector $\text{AN-RFMSE}_{\text{vec}}$. Moreover, the size of the training sets are indicated on the x-axis of the subplots. The blue bar shows the median AN-RFMSE among 20 sparse DNN models over 20 test sets. The orange bar shows the median AN-RFMSE among 20 dense DNN models over 20 test sets. For each subfigure, the $\overline{\text{AN-RFMSE}}$ are calculated for a given number of timesteps reported in the captions of each subfigure (14a - 14d). Notice the logarithmic scale of the y-axis.

Fig. 14 contains a good amount of information about the model performance of dense and sparse DNN models. Figs. 14a to 14d report median and extreme values of $\text{AN-RFMSE}_{\text{vec}}$ over four different time horizons for five groups of models trained on five data sets with different sizes. Hence, the results in Fig. 14 show how dense and sparse DNN models perform with varying amounts of training data over varying time horizons. Figs. 14a to 14d show that the groups of **sparse models** trained on data sets with varying size show similar results, both in terms of median AN-RFMSE and extreme values. However, as Fig. 14d shows, there seems to be a small trend that groups with more training data perform slightly better over longer forecasting horizons. Furthermore, the band between the minimum and maximum values of AN-RFMSE is overall relatively small for all groups of models and all forecast horizons for sparse models. The converging behavior of the performance of groups of sparse models as a function of the amount of data in the training set indicates that only small amounts of data are required to gain significance for the model parameters. While the sparse models show stable performance across groups of models with different amounts of training data and slowly increasing values of AN-RFMSE proportional to the length of the forecasting horizon, the same cannot be said about the performance of the dense models. When considering the **dense models**, Figs. 14a to 14d indicate that there is a trend where both median, minimum and maximum values of AN-RFMSE decreases significantly as sizes of training set decreases. This expected trend indicates that the performance improves with increasing dataset size. However, the trend is not consistent for all groups of dense DNN models for all forecasting horizons. Furthermore, the maximum values of AN-RFMSE for groups of dense DNN models for longer forecasting horizons such as in Fig. 14c and Fig. 14d show that AN-RFMSE exponentially increases for some of the models within the groups. This indicates that the dense DNN models are likely to have some input regions where the model output is not sound. If the model estimate enters a region with poorly modeled dynamics, the model estimate might drift exponentially. For short-term prediction, that is in Fig. 14a and Fig. 14b, the trend is that dense models show better performance for median and minimum values, especially within the groups with large training sets. This may be because dense models have more flexibility in terms of more parameters. Furthermore, the sparse regularizers defined in Section 2.2 are guiding the structure of the network. Sparse regularizers are based on assumptions about the model structure that might ignore some of the dynamics in the system. However, for longer forecasting horizons (Fig. 14c and Fig. 14d), sparse models are always showing better performance than dense models in terms of median AN-RFMSE . This is a typical example of a bias-variance trade-off. For all forecasting horizons and within all groups of training set sizes, sparse models are always showing a smaller maximum value of AN-RFMSE .

4.3. Training stability perspective

Sparsification on a large ensemble of neural networks gives similar sparse structures. This has been shown in the structure plots in the Figs.4-11. Furthermore, Table 5 show that sparse models to a large extent finds the same feature basis for each of the model outputs $\{\hat{f}_1, \dots, \hat{f}_8\}$.

Moreover, Fig. 14 clearly indicates for all forecasting horizons that the uncertainty bounds for dense models are much larger than those for sparse models. For the longer horizons, some of the dense models tend to blow up. This is probably due to that the model enters a region of the input space where it overfits. This can be seen as poor generalization to that specific area. However, for shorter prediction horizons such as in Fig.14a, the large bound between minimum and maximum AN-RFMSE is not of an order that indicates a blow up. Still, this uncertainty bounds are larger for dense models than for sparse models. This indicates that the sparse models are more likely to converge to a similar minimum than the dense models. The results presented in Fig. 14 also indicates that the sparse models are likely to converge already for small amounts of data. This is not the case for dense models.

5. Conclusions and future work

This article presents a sparse neural network model that approximates a set of nonlinear ODEs based on time series data sampled from the system variables included in the ODEs. The set of nonlinear ODEs represents an aluminum electrolysis simulator based on the mass and energy balance of the process. This includes nonlinear and interrelated models of electrochemical and thermal subprocesses. The sparsity in the model is achieved by imposing sparsity using ℓ_1 regularization on the weights. The main takeaway from the work can be concluded as follows:

- ℓ_1 regularization drastically reduces the number of parameters in the DNN. In our case we witnessed a 93% reduction in the parameters compared to the corresponding dense neural network.

- The sparse neural network was more interpretable using the domain knowledge of the aluminium electrolysis process. In contrast the dense neural networks were completely black-box.
- Sparse neural networks were consistently more stable compared to the dense counterparts. This was reflected in the model uncertainty estimates based on a large ensemble of models.
- For short prediction horizon, the median accuracy of dense models are better than for sparse models. However, the uncertainty bounds of dense models are much larger.
- For longer prediction horizons, sparse models outperforms dense models both in terms of higher median accuracy and lower uncertainty bounds.

While these sparse models show promising results within interpretability and generalizability, there is still a high potential for improvement. There is a desire to increase prediction accuracy and decrease the bias of the sparse models. This might be addressed by investigating other sparsity structures at different layers that better compromise the bias-variance trade-off. One possible direction is to inject simplified theories known from first principle into the neural network to possibly increase accuracy.

6. Acknowledgments

This work was supported by the industry partners Borregaard, Elkem, Hydro, Yara and the Research Council of Norway through the project TAPI: Towards Autonomy in Process Industries, project number 294544.

References

- [1] K. Grotheim, H. Kvande, *Introduction to Aluminium Electrolysis-Understanding the Hall-Heroult Process*, Aluminium-Verlag, Dusseldorf, Germany, 1993.
- [2] V. Gusberti, D. S. Severo, B. J. Welch, M. Skyllas-Kazacos, Modeling the mass and energy balance of different aluminium smelting cell technologies, in: *Light Metals 2012*, Springer, 2012, pp. 929–934.
- [3] K. E. Einarssrud, I. Eick, W. Bai, Y. Feng, J. Hua, P. J. Witt, Towards a coupled multi-scale, multi-physics simulation framework for aluminium electrolysis, *Applied Mathematical Modelling* 44 (2017) 3–24.
- [4] P. Mandin, R. Wüthrich, H. Roustan, Industrial aluminium production: the hall-heroult process modelling, *ECS Transactions* 19 (26) (2009) 1.
- [5] A. Naimi, J. Deng, A. Abdulrahman, V. Vajpayee, V. Becerra, N. Bausch, Dynamic neural network-based system identification of a pressurized water reactor, 2020, p. 100 – 104.
- [6] E. M. Rentería-Vargas, C. J. Zúñiga Aguilar, J. Y. Rumbo Morales, F. D. J. S. Vázquez, M. De-La-Torre, J. A. Cervantes, E. S. Bustos, M. Calixto Rodríguez, Neural network-based identification of a psa process for production and purification of bioethanol, *IEEE Access* 10 (2022) 27771–27782.
- [7] D. Fooshee, A. Mood, E. Gutman, M. Tavakoli, G. Urban, F. Liu, N. Huynh, D. Van Vranken, P. Baldi, Deep learning for chemical reaction prediction, *Mol. Syst. Des. Eng.* 3 (2018) 442–452.
- [8] S. S. Blakseth, A. Rasheed, T. Kvamsdal, O. San, Deep neural network enabled corrective source term approach to hybrid analysis and modeling, *Neural Networks* 146 (2022) 181–199.
- [9] O. San, A. Rasheed, T. Kvamsdal, Hybrid analysis and modeling, eclecticism, and multifidelity computing toward digital twin revolution (2021). [arXiv:2103.14629](https://arxiv.org/abs/2103.14629).
- [10] Y. Zhang, P. Tiño, A. Leonardis, K. Tang, A survey on neural network interpretability (2021). [arXiv:2012.14261](https://arxiv.org/abs/2012.14261).
- [11] E. T. B. Lundby, A. Rasheed, J. T. Gravdahl, I. J. Halvorsen, A novel hybrid analysis and modeling approach applied to aluminum electrolysis process, *Journal of Process Control* 105 (2021) 62–77.
- [12] M. Raissi, P. Perdikaris, G. Karniadakis, Physics-informed neural networks: A deep learning framework for solving forward and inverse problems involving nonlinear partial differential equations, *Journal of Computational Physics* 378 (2019) 686–707.
- [13] S. Pawar, O. San, B. Aksoylu, A. Rasheed, T. Kvamsdal, Physics guided machine learning using simplified theories, *Physics of Fluids* 33 (1) (2021) 011701.
- [14] P. R. Chermont, F. M. Soares, R. C. De Oliveira, Simulations on the bath chemistry variables using neural networks, in: *TMS Light Metals*, Vol. 2016-January, 2016.
- [15] A. M. F. de Souza, F. M. Soares, M. A. G. de Castro, N. F. Nagem, A. H. d. J. Bitencourt, C. d. M. Affonso, R. C. L. de Oliveira, Soft sensors in the primary aluminum production process based on neural networks using clustering methods, *Sensors* 19 (23) (2019).
- [16] D. Bhattacharyay, D. Kocae, Y. Kocae, B. Morais, An artificial neural network model for predicting the co 2 reactivity of carbon anodes used in the primary aluminum production, *Neural computing and Applications* 28 (3) (2017) 553–563.
- [17] I. Goodfellow, Y. Bengio, A. Courville, *Deep learning*, MIT press, 2016.
- [18] J. Frankle, M. Carbin, The lottery ticket hypothesis: Finding sparse, trainable neural networks, *arXiv preprint arXiv:1803.03635* (2018).
- [19] B. K. Natarajan, Sparse approximate solutions to linear systems, *SIAM journal on computing* 24 (2) (1995) 227–234.

- [20] G. F. Montufar, R. Pascanu, K. Cho, Y. Bengio, On the number of linear regions of deep neural networks, in: Z. Ghahramani, M. Welling, C. Cortes, N. Lawrence, K. Q. Weinberger (Eds.), Advances in Neural Information Processing Systems, Vol. 27, Curran Associates, Inc., 2014.
- [21] R. Pascanu, G. Montufar, Y. Bengio, On the number of response regions of deep feed forward networks with piece-wise linear activations, ICLR, 2014.
- [22] T. Serra, C. Tjandraatmadja, S. Ramalingam, Bounding and counting linear regions of deep neural networks, CoRR abs/1711.02114 (2017). [arXiv:1711.02114](https://arxiv.org/abs/1711.02114).
- [23] 14 - general physical properties, in: W. Gale, T. Totemeier (Eds.), Smithells Metals Reference Book (Eighth Edition), eighth edition Edition, Butterworth-Heinemann, Oxford, 2004, pp. 14–1–14–45.
- [24] I. Dincer, C. Zamfirescu, Chapter 1 - fundamentals of thermodynamics, in: I. Dincer, C. Zamfirescu (Eds.), Advanced Power Generation Systems, Elsevier, Boston, 2014, pp. 1–53.
- [25] S. Skogestad, Chemical and energy process engineering, CRC press, 2008.
- [26] A dynamic model for the energy balance of an electrolysis cell, Chemical Engineering Research and Design 74 (8) (1996) 913–933.
- [27] T. Drengstig, On process model representation and al₃ dynamics of aluminum electrolysis cells, Ph.D. thesis, Ph. D. thesis, Norwegian Univ. of Science and Tech.(NUST) (1997).
- [28] S. W. Jessen, Mathematical modeling of a hall hérault aluminium reduction cell, Master's thesis, Technical University of Denmark, DTU, DK-2800 Kgs. Lyngby, Denmark (2008).
- [29] T. M. Hyde, B. J. Welch, The gas under anodes in aluminium smelting cells. part i: Measuring and modelling bubble resistance under horizontally oriented electrodes, LIGHT METALS-WARRENDALE- (1997) 333–340.
- [30] A. Solheim, S. Rolseth, E. Skybakmoen, L. Støen, Å. Sterten, T. Støre, Liquidus temperature and alumina solubility in the system na 3 al₂o₃-al₂o₃-ca₂o₃-mg₂o₃ 2, in: Essential Readings in Light Metals: Aluminum Reduction Technology, Volume 2, John Wiley & Sons, 2013, pp. 73–82.

Appendix A. Simulation model

In this section we will follow a purely physics-based approach to deriving the equations. At appropriate places we will highlight the challenges and assumption

The dynamical system simulated in this study is generated by the set of ordinary differential equations (ODE's) in Eqs. (17) - (24). This system of equations is derived from a simplified model of an aluminum electrolysis cell. This model comprises simplified energy and mass balance of the electrolysis cell. The model consider an energy balance based on sideways heat transfer, energy transfer between side ledge and bath due to melting and freezing of cryolite, and energy input as a function of electrical resistance in the electrolyte and voltage drop due to bubbles. The mass balance includes mass transfer between side ledge and bath, input of Al_2O_3 and AlF_3 , production of metal and consumption of the raw material Al_2O_3 and tapping of metal from the electrolysis cell. In Table 1, the system states and inputs are described. The purpose of the simulation model is not to mimic the exact dynamics of an aluminum electrolysis cell, but rather to generate nonlinear dynamics similar to what occurs in a real aluminum electrolysis.

Appendix A.1. Heat capacity

Heat capacity is a measure of the amount of thermal energy a body of a certain material can store for a given temperature and volume and is given by the definition [23]:

$$C = \frac{\delta q}{\delta T}. \quad (A.1)$$

$C[J/\text{°C}]$ is the heat capacity, $\delta q[J]$ is an infinitesimal heat quantity and $\delta T[\text{°C}]$. Specific heat capacity c_p is heat capacity at constant pressure per unit of mass:

$$c_p = \left(\frac{dh}{dT} \right)_p, \quad (A.2)$$

where $c_p [J/(kg\text{°C})]$ is the specific heat capacity, $h [J/kg]$ is specific enthalpy and $T [\text{°C}]$ is temperature. The subscript p indicates constant pressure. In the process of aluminum electrolysis, the pressure can be assumed to be constant at $p = 1 [\text{atm}]$.

Appendix A.2. Energy and mass balance

The first law of thermodynamics known as the energy conservation principle states the following [24]:

$$\frac{dE_i}{dt} = \dot{E}_{in, i} - \dot{E}_{out, i}. \quad (A.3)$$

$\frac{dE_i}{dt} [W]$ is the change of energy of species i in the system, $\dot{E}_{in, i} [W]$ is the energy input rate and $\dot{E}_{out, i} [W]$ is the energy output rate of species i the system. System is here used synonymous to control volume. The energy of the system can be transferred through heat, work or through the energy associated with the mass crossing the system boundary. This can be expressed as follows:

$$\dot{E}_{in, i} = \dot{Q}_{in, i} + \dot{W}_{in, i} + \dot{m}_{in, i}e_{in, i} \quad (A.4)$$

$$\dot{E}_{out, i} = \dot{Q}_{out, i} + \dot{W}_{out, i} + \dot{m}_{out, i}e_{out, i} \quad (A.5)$$

where $\dot{Q}_{in, i} [W]$ and $\dot{Q}_{out, i} [W]$ are the rates of heat in and out of the system and $\dot{W}_{in, i} [W]$ and $\dot{W}_{out, i} [W]$ is the rate of work generated on the system. $\dot{m}_{in, i} [kg/s]$ and $\dot{m}_{out, i} [kg/s]$ is the mass rate into the system and out of the system respectively, whereas $e_{in, i} [J/kg]$ and $e_{out, i} [J/kg]$ is the specific energy of the mass entering and leaving the system. The specific energy can be formulated as:

$$e = u + \frac{1}{2}v^2 + gz, \quad (A.6)$$

where $u [J/kg]$ is the specific internal energy, $\frac{1}{2}v^2 [J/kg]$ is the specific energy related to velocity $v [m/s]$, and $gz [J/kg]$ is the specific energy related to elevation difference $z [m]$.

The change of system energy $\frac{dE_i}{dt} = \dot{E}_i$ can be written as:

$$\frac{dE_i}{dt} = \frac{d(m_i e_i)}{dt}, \quad (\text{A.7})$$

where m [kg] is the mass of the system and e_i [J/kg] is the specific energy of the system. Since the relevant control volumes are related to an aluminum electrolysis, it is reasonable to neglect the terms $\frac{1}{2}v^2$ and gz . In this work, $\dot{Q} = Q_{in, i} - Q_{out, i}$ is defined as positive when net heat is provided to the system, and $W = W_{in, i} - W_{out, i}$ is positive when work is added to the system. Thus, the resulting energy equation can be formulated as:

$$\frac{d(m_i u_i)}{dt} = m \frac{du_i}{dt} + u_i \frac{dm_i}{dt} = \dot{m}_{in, i} u_{in, i} - \dot{m}_{out, i} u_{out, i} + \dot{Q} + \dot{W}. \quad (\text{A.8})$$

Work W [J] is organized transfer of energy. W can be divided into several types of work [25]:

$$W = W_{flow} + W_{\Delta V} + W_s + W_{el} + W_{other}. \quad (\text{A.9})$$

W_{flow} is the work associated with the volume displacements of streams that enter and exit the system, $W_{\Delta V}$ is the work associated with changes of the volume of the system, W_s is the mechanical work supplied using movable machinery, W_{el} is the electrochemical work supplied when the system is connected to an external electric circuit. W_{other} is the sum of other types of work, for example if surface areas changes or electromagnetic work. For an aluminum electrolysis, $W_{\Delta V} = W_s = W_{other} \approx 0$. W_{flow} is given by:

$$W_{flow} = pV, \quad (\text{A.10})$$

where p is pressure and V is volume. Enthalpy H [J] is given by:

$$H = U + pV. \quad (\text{A.11})$$

where $U = m \cdot u$ [J]. Furthermore, $H = h \cdot m$. Thus:

$$m \frac{du_i}{dt} + u_i \frac{dm_i}{dt} = \dot{m}_{in, i} h_{in, i} - \dot{m}_{out, i} h_{out, i} + \dot{Q} + \dot{W}_{el}. \quad (\text{A.12})$$

Assuming that the flow work is neglectable compared to the other quantities in the energy equation for aluminum electrolysis gives that $H \approx U$. Recall that $c_p = \frac{dh}{dT}$. Hence:

$$\frac{du_i}{dt} \approx \frac{dh_i}{dt} = \frac{\partial h_i}{\partial T_i} \frac{dT_i}{dt} = c_{p_i} \frac{dT_i}{dt}, \quad (\text{A.13})$$

where $\frac{dT}{dt} = \dot{T}_i$ [$^{\circ}\text{C}$] is the temperature derivative with respect to time. This yields:

$$\frac{dT_i}{dt} = \frac{1}{m_i c_{p_i}} \left(\dot{m}_{in, i} h_{in, i} - \dot{m}_{out, i} h_{out, i} + \dot{Q} + \dot{W}_{el} - u_i \frac{dm_i}{dt} \right) \quad (\text{A.14})$$

The mass rate equation can be formulated as:

$$\frac{dm_i}{dt} = \dot{m}_{in} - \dot{m}_{out} + \sum_{j=1}^{n_j} r_{i,j}, \quad (\text{A.15})$$

where $r_{i,j}$ is the reaction rate of species i being produced or consumed in reaction j . Assuming that the contents of the control volume to be perfectly mixed and assuming that the flow work is neglectable gives:

$$u_i \approx h_i = h_{out, i}. \quad (\text{A.16})$$

Hence, the resulting temperature specific energy equation for component i in a control volume is given by:

$$\frac{dT_i}{dt} = \frac{1}{m_i c_{p_i}} \left(\dot{m}_{in,i} (h_{in,i} - h_{out,i}) + \dot{Q} + \dot{W}_{el} - h_{out,i} \sum_{j=1}^{n_j} r_{i,j} \right) \quad (\text{A.17})$$

The latter equation states that the time derivative of the temperature in the control volume is dependent on the composition of species in the control volume. It is assumed that the temperature is equal for all components in the control volume. Furthermore, it is assumed that there is a common heat loss \dot{Q} from a control volume to other control volumes, and that electrical power \dot{W}_{el} is performed on the whole control volume instead of on different components in the control volume. When different components are mixed in a control volume, the enthalpy of this mix is more complex than adding the enthalpy of individual species. However, the complexity of mixed enthalpy is left out of this simulation model. The heat capacity of a mix of components in a control volume $c_{p_{cv}}$ is simplified to be constant despite of that $c_{p_{cv}}$ varies with composition and temperature in the control volume. The values for different species and control volumes are taken from [26] and [27]. Thus, the simplified simulation equation for the temperature derivative in a control volume is given by:

$$\frac{dT_{cv}}{dt} = \frac{1}{m_{cv} c_{p_{cv}}} \left(\left[\sum_{i=1}^{n_i} \dot{m}_{in,i} (h_{in,i} - h_{out,i}) \right] + \dot{Q} + \dot{W}_{el} - \sum_{i=1}^{n_i} \left[h_{out,i} \sum_{j=1}^{n_j} r_{i,j} \right] \right) \quad (\text{A.18})$$

where m_{cv} is the sum of masses in the control volume.

Appendix A.3. Heat transfer

Heat transfer $\dot{Q}[W]$ will from this point be referred to as Q , meaning that the dot is omitted. In the process of aluminum electrolysis, the two most important principles for heat transfer are convection and conduction. **Conduction** is heat transfer through molecular motion within a solid material. The expression for conduction is given by

$$Q = -k \cdot A \cdot \frac{\partial T}{\partial x}. \quad (\text{A.19})$$

Q [W] is heat transferred, A [m^2] is the area the heat is transferred through, $\frac{\partial T}{\partial x}$ [$^{\circ}\text{C}/m$] is the temperature gradient in the direction x that the heat is transferred, and k [$W/(m^{\circ}\text{C})$] is the thermal conductivity, a material dependent proportionality constant. For a fixed cross-section area, the one dimensional **steady state heat flow** through a wall of thickness x [m] from $x = 0$ with temperature T_1 to $x = 1$ with temperature T_1 integrates to:

$$Q = k \cdot A \cdot \frac{T_1 - T_2}{x}, \quad (\text{A.20})$$

where $T_1 > T_2$. Thermal conductive resistance for a plane wall can be extracted from the latter expression:

$$R_{cond} = \frac{x}{k \cdot A}, \quad (\text{A.21})$$

where R_{cond} [$^{\circ}\text{C}/W$] is the thermal resistance, x [m] is the thickness of the solid material in the direction heat is transferred, and k and A are as mentioned above. Thermal conductive analysis is analogous to an electrical circuit, where the temperature difference is analogous to the potential difference V , the heat flow is analogous to the electrical current I and thermal resistance is analogous to electrical resistance R_{el} . **Convection** is the heat transfer through the mass motion of a fluid. Heat transfer between a surface at temperature T_s and a fluid at a bulk temperature T_f is due to convection. Convection can be formulated as:

$$Q = h \cdot A \cdot (T_s - T_f), \quad (\text{A.22})$$

where $A[m^2]$ is the contact surface between a solid surface and the liquid, the the heat transfer coefficient $h [W/(m^2)^\circ C]$ is the proportionality constant between the heat flux and the thermodynamic driving force for the flow of heat, i.e. the temperature difference $(T_s - T_f)$.

Thermal resistance can be defined for a fluid R_{conv} , and is given by:

$$R_{conv} = \frac{1}{h \cdot A}. \quad (\text{A.23})$$

As for electrical circuits, thermal resistances can be coupled in series, and the reciprocal of the total resistance equals the sum of reciprocals of individual resistances:

$$\frac{1}{R_{tot}} = \sum_{i=1}^N \frac{1}{R_i} \quad (\text{A.24})$$

Eq. A.24 together with the assumption of stationary heat transfer makes it possible to calculate the heat transfer from one edge to the other through several resistors in series as the temperature difference between the edges divided by the sum of reciprocals of individual resistors:

$$Q = \frac{T_1 - T_{N+1}}{\sum_{i=1}^N R_i}, \quad (\text{A.25})$$

where $T_1 > T_2 > \dots > T_{N+1}$ is temperature and R_i are the resistors. In the simulation model, the heat transfer is assumed to be piecewise stationary, meaning that the heat transfer is assumed to be constant from the middle of one control volume to the middle of the adjacent control volume. However, the heat transfer is not assumed to be stationary through several control volumes. Thus, there are separate energy balances for each control volume. Heat transfer is only considered through the side walls of the electrolysis cell.

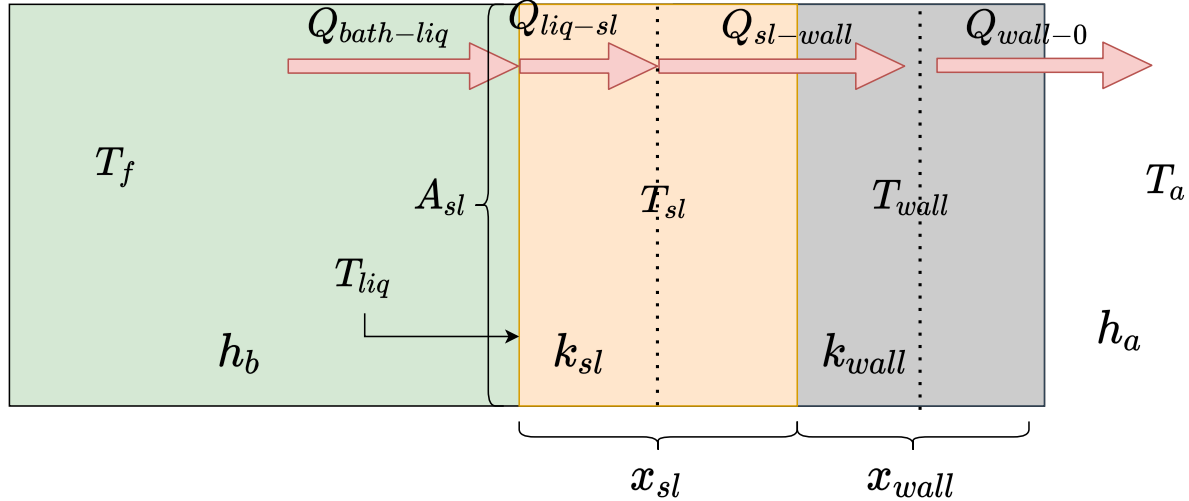


Figure A.15: Convection and conduction trough several materials

Convective heat transfer $Q_{bath-liq}$ from the bath to the surface of the side ledge

$$Q_{bath-liq} = h_{bath-sl} A_{sl} (T_{bath} - T_{liq}). \quad (\text{A.26})$$

Conductive transfer Q_{liq-sl} from surface of side ledge to the center of the side ledge

$$Q_{liq-sl} = \frac{2k_{sl}A_{sl}(T_{liq} - T_{sl})}{x_{sl}}. \quad (\text{A.27})$$

Conductive heat transfer $Q_{sl-wall}$ from center of side ledge to the center of the side wall

$$Q_{sl-wall} = \frac{A_{sl}(T_{sl} - T_{wall})}{(x_{wall}/2k_{wall}) + (x_{sl}/2k_{sl})} \quad (\text{A.28})$$

The heat transfer from the middle of the wall to the ambient Q_{wall-0} consists of conductive heat transfer from the middle of the wall to the surface of the wall, and the convection from the surface of the wall to the ambient air

$$Q_{wall-0} = \frac{A_{sl}(T_{wall} - T_0)}{(1/h_{wall-0}) + (x_{wall}/2k_{wall})}. \quad (\text{A.29})$$

Appendix A.4. Electrochemical power

Electrochemical power \dot{W}_{el} [W], from now referred to as P_{el} is the amount of energy transferred to a system from a electrical circuit and is defined as:

$$P_{el} = U_{cell} \cdot I_{line}, \quad (\text{A.30})$$

where U_{cell} [V] is the applied cell voltage and I_{line} [A] is the line current sent through the electrolyte. The cell voltage is composed of three different types of voltage contributions. these are the **decomposition voltage**, which is the theoretical minimum potential for the decomposition of alumina, **overvoltage**, meaning the excess voltage due to electrode polarization and **ohmic voltage drops**, due to resistance of various sections in the cell [28]. These contributions can be divided into smaller contributions caused by different effects in different parts of the cells. To make the mathematical expression in the resulting nonlinear simulation model less comprehensive, only **ohmic voltage drop** contributions are included. These are:

- Electrolyte voltage drop U_{el} [V]
- Bubble voltage drop U_{bub} [V]

The **voltage drop over the electrolyte** is due to the electrical resistivity of the electrolyte. Assuming uniform current density, the resistance of the elecrolyte is given by:

$$R_{el} = \frac{1}{\kappa} \frac{d}{A}. \quad (\text{A.31})$$

R_{el} [Ω] is the electrical resistance, κ [$1/(\Omega m)$] is electrical conductivity, d [m] is the interpolar distance and A [m^2] is the total surface of the anodes. The expression for electrical conductivity is given by [1]:

$$\kappa = \exp \left(2.0156 - \frac{2068.4}{T_{bath} + 273} + 0.4349 \cdot BR - 2.07C_{Al_2O_3} - 0.5C_{CaF_2} - 1.66C_{MgF_2} + 1.78C_{LiF} + 0.77C_{Li_3AlF_6} \right). \quad (\text{A.32})$$

T_{bath} [$^{\circ}C$] is the temperature of the electrolyte, BR [–] is the bath ratio, while C_x [–] is the concentration of substance x . BR is assumed to be constant at 1.2, $C_{MgF_2} = 0.01$, $C_{CaF_2} = 0.05$, $C_{LiF} = 0$ and $C_{Li_3AlF_6} = 0$. Thus, κ can be simplified to:

$$\kappa = \exp \left(2.496 - \frac{2068.4}{T_{bath} + 273} - 2.07C_{Al_2O_3} \right). \quad (\text{A.33})$$

The voltage drop due to resistance in the electrolyte is given by:

$$U_{EL} = R_{EL} \cdot I_{line} \quad (\text{A.34})$$

Gas accumulation beneath the anode surface which reduces the cross-sectional area of the electrolyte in that zone. Thus, the effective resistivity increases and causes the so called **bubble voltage drop** U_{bub} [29]:

$$U_{bub} = \frac{d_{bub} \cdot j_A}{\kappa} \frac{\phi}{1 - \phi}. \quad (\text{A.35})$$

j_A [A/cm^2] is the anode current density d_{bub} [cm] in the bubble layer thickness and ϕ [–] is the bubble coverage as a fraction of the anode:

$$d_{bub} = \frac{0.5517 + j_A}{1 + 2.167j_A}, \quad (\text{A.36})$$

and

$$\begin{aligned} \phi = & 0.509 + 0.1823j_A - 0.1723j_A^2 + 0.05504j_A^3 \\ & + \frac{0.4322 - 0.3781BR}{1 - 1.637BR} + \frac{0.431 - 0.1437(x_{Al_2O_3} - x_{Al_2O_3}^{AE})}{1 + 7.353(x_{Al_2O_3} - x_{Al_2O_3}^{AE})} \end{aligned} \quad (\text{A.37})$$

$x_{Al_2O_3}$ [–] is the weight percent of alumina in the bath and $x_{Al_2O_3}^{AE}$ [–] is the weight percent of alumina at where the anode effect occurs, in this case it is assumed that $x_{Al_2O_3}^{AE} = 2.0$. Since the simulation model is simplified to only include contributions from U_{bub} and U_{EL} , the total applied cell voltage in the simulation model is given by:

$$U_{cell} = U_{EL} + U_{bub}. \quad (\text{A.38})$$

Appendix A.5. Mass rates

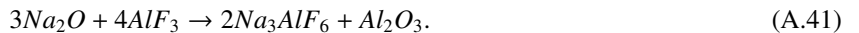
The substances considered in the simulation model are alumina (Al_2O_3), aluminum fluoride (AlF_3) and cryolite (Na_3AlF_6) in the bath and liquid aluminum (Al) in the metal pad below the bath. Aluminum is extracted from alumina, which is dissolved in the electrolytic bath. In addition to alumina, carbon anodes are consumed in the net reaction, producing molten aluminum and carbon dioxide gas (CO_2):



This reaction occurs at a rate according to Faraday's law for aluminum electrolysis [27]:

$$r_{al} = \frac{CE \cdot I_{line}}{z \cdot F}, \quad (\text{A.40})$$

where r_{al} [mol/s] is the reaction rate of the primary reaction of the Hall-Héroult process presented in Eq. A.39, $z = 12$ is the number of electrons in the reaction, $F = 96486.7[(A \cdot s)/mol]$ is the Faraday constant, and CE [–] is the current efficiency, assumed constant at $CE = 0.95$. The fed alumina contains several impurities [27]. In the simulation model derived used in this work, only sodium oxide (Na_2O) is considered as additions in the feeded alumina. The content of Na_2O in alumina react as:



3 Mol Na_2O reacts with 4 Mol of AlF_3 and produces 2 Mol of Na_3AlF_6 and 1 Mol of Al_2O_3 . The reaction rate of the latter reaction r_{bath} [$kmol/s$] can be formulated as:

$$r_{bath} = \frac{C_{Na_2O}}{3M_{Na_2O}} u_{Al_2O_3}, \quad (\text{A.42})$$

where C_{Na_2O} [–] is the weight percent of Na_2O in the alumina feed, M_{Na_2O} [g/mol] is the molar mass of Na_2O and $u_{Al_2O_3}$ kg/s is the rate of alumina feed. The reaction in Eq. A.41 affects the mass balance of both AlF_3 , Na_3AlF_6 and Al_2O_3 . Therefore, r_{bath} is included in the mass balance equations of all these species. The general mass rate Eq. A.15 is used in the derivation the mass rate of side ledge, cryolite, alumina, aluminum fluoride and metal. The control volumes in which there are nonzero mass rates are the bath/electrolyte, the metal pad and the side ledge. The **mass**

rates in the electrolyte are:

$$\dot{m}_{Al_2O_3} = (1 - C_{Na_2O})u_{Al_2O_3} - \frac{2}{1000}r_{al}M_{Al_2O_3} + r_{bath}M_{Al_2O_3}. \quad (A.43)$$

$\dot{m}_{Al_2O_3}$ [kg/s] is the mass rate of alumina and $M_{Al_2O_3}$ [g/mol] is the molar mass of alumina. $\frac{2}{1000}r_{al}M_{Al_2O_3}$ [kg/s] is the reaction rate of alumina produced due to the reaction in Eq. A.39 and $r_{bath}M_{Al_2O_3}$ [kg/s] is the reaction rate of alumina due to the reaction in Eq. A.41. The mass rate of AlF_3 is given by:

$$\dot{m}_{AlF_3} = u_{AlF_3} - 4r_{bath}M_{AlF_3}, \quad (A.44)$$

where \dot{m}_{AlF_3} [kg/s] is the mass rate of aluminum fluoride, u_{AlF_3} [kg/s] is the input rate of aluminum fluoride and $4r_{bath}M_{AlF_3}$ [kg/s] is the reaction rate of produced aluminum fluoride from the reaction in equation (A.41). The mass rate of cryolite in the bath is given by:

$$\dot{m}_{cry} = w_{fus} + 2r_{bath}M_{cry}. \quad (A.45)$$

\dot{m}_{cry} [kg/s] is the mass rate of cryolite in the electrolyte, $2r_{bath}M_{cry}$ [kg/s] is the reaction rate of produced cryolite due to the reaction in Eq. A.41 and w_{fus} [kg/s] is the mass rate of cryolite transferred between the side ledge and the bath. w_{fus} is given by:

$$w_{fus} = \frac{Q_{bath-liq} - Q_{liq-sl}}{\Delta_{fus}H_{cry}}. \quad (A.46)$$

$Q_{bath-liq}$ and Q_{liq-sl} is given in Eqs. A.26 and (A.27) respectively and $\Delta_{fus}H_{cry}$ is the heat of fusion for cryolite, i.e. the amount of energy required to melt one kg of cryolite. The heat of fusion for cryolite at 1000°C is $\Delta_{fus}H_{cry} = 119495$ [J/kg] [27], and is assumed to be constant in the simulation model. The **side ledge** is necessary to withstand the highly corrosive molten cryolite in the oven. The side ledge consists of *frozen* cryolite [27]. The mass rate of side ledge is therefore the transfer of cryolite between the electrolyte and side ledge due to melting and freezing:

$$\dot{m}_{sl} = -w_{fus}. \quad (A.47)$$

\dot{m}_{sl} [kg/s] is the mass rate of side ledge, and w_{fus} [kg/s] is given above. The **mass rate of aluminum** is given by:

$$\dot{m}_{Al} = \frac{2}{1000}r_{al}M_{Al} - u_{tap}. \quad (A.48)$$

\dot{m}_{Al} [kg/s] is the mass rate of aluminum, $\frac{2}{1000}r_{al}M_{Al}$ [kg/s] is the reaction rate of produced aluminum due to the reaction in equation (A.39), and u_{tap} [kg/s] is the control input of tapping metal from the oven.

Appendix A.6. Temperature derivatives

Eq. (A.18) is used to calculate the temperature derivatives in the electrolyte, side ledge and side wall. As mentioned above, $\dot{Q} = Q$ and $\dot{W}_{el} = P_{el}$. In the **electrolyte**, the energy is transferred in and out of the control volume in many different ways. Heat $Q_{bath-sl}$ is transferred through convection from the bath to the side ledge surface ($Q_{bath-liq}$) and from the side ledge surface to the center of the side ledge with conductive heat Q_{liq-sl} . The resulting heat transfer can be formulated as:

$$Q_{bath-sl} = \frac{T_{bath} - T_{sl}}{(x_{sl}/2k_{sl}A_{sl}) + 1/(h_{bath-sl}A_{sl})}. \quad (A.49)$$

Energy is transferred through mass transfer in several ways. Energy needed to heat and melt substances fed as control input u is given by:

$$E_u = \Delta_{fus}H_{Al_2O_3}u_{Al_2O_3} + \Delta_{fus}H_{AlF_3}u_{AlF_3} + (T_{bath} - T_{in})(\bar{c}_{p_{Al_2O_3}}u_{Al_2O_3} + \bar{c}_{p_{AlF_3}}u_{AlF_3}). \quad (A.50)$$

$\Delta_{fus}H_i$ [J/kg] is the specific heat of fusion for substance i , and \bar{c}_{p_i} [J/(°Ckg)] is the average heat capacity from T_{in} to T_{bath} . Energy is also transferred through mass transfer between the electrolyte and the side ledge. When side ledge

(frozen cryolite) melts into the bath, energy is required both to heat and melt the frozen cryolite. The energy required to heat the frozen cryolite is:

$$E_{tc, liq} = w_{fus} c_{p, cry, liq} (T_{bath} - T_{liq}). \quad (\text{A.51})$$

w_{fus} [kg/s] is as mentioned above the mass rate of cryolite between bath and side ledge, and is positive when cryolite melts and is transferred to the bath. $c_{p, cry, liq}$ [J/(°C kg)] is the heat capacity of molten cryolite T_{bath} [°C] is the bath temperature and T_{liq} [°C] is the liquidus temperature at which cryolite melts and freezes. $E_{tc, liq}$ [W] is the energy required to heat molten cryolite from liquidus temperature to bath temperature. The subscript tc stands for temperature change and the subscript liq indicates that the substance is liquid. When $E_{tc, liq}$ is positive, it is because w_{fus} is positive, indicating that cryolite is melting. Thus, when $E_{tc, liq}$ is negative, cryolite is freezing. The energy needed to melt frozen cryolite is given by:

$$E_{sc} = w_{fus} \Delta_{fus} H_{cry}. \quad (\text{A.52})$$

E_{sc} [W] is the energy required to melt the mass of frozen electrolyte. The subscript sc stands for state change, meaning that it transitions between solid and liquid. $\Delta_{fus} H_{cry}$ [J/kg] is the heat of fusion for cryolite as mentioned above. When E_{sc} is positive, cryolite is melted and energy is required whereas when E_{sc} is negative, cryolite freezes, and energy is released. Energy is required for the primary reaction in Eq. A.39 since it is endothermic:

$$E_{r_{al}} = r_{al} \Delta H_{r_{al}}. \quad (\text{A.53})$$

$E_{r_{al}}$ [W] is the amount of energy required for the reaction to take place, r_{al} [mol/s] is as mentioned above the reaction rate of the primary reaction in the process, and $\Delta H_{r_{al}} = 2197582$ [J/mol] is the enthalpy of reaction for (A.39). Since the reaction in equation (A.41) is exothermic, this reaction releases energy to its surroundings. This is given by:

$$E_{r_{bath}} = 1000 r_{bath} \Delta H_{r_{bath}}. \quad (\text{A.54})$$

$E_{r_{bath}}$ [W] is the energy released due to the reaction in (A.41) r_{bath} [kmol/s] = 1000 [mol/s] is the reaction rate of (A.41) and $\Delta H_{r_{bath}} = -993283$ [J/mol] is the enthalpy of reaction for (A.41). The time derivative for the bath temperature is given by:

$$\dot{T}_{bath} = \frac{P_{el} - Q_{bath-sl} - E_u - E_{tc, liq} - E_{sc} - E_{r_{al}} - E_{r_{bath}}}{m_{bath} c_{p_{bath, liq}}}. \quad (\text{A.55})$$

m_{bath} [kg] is the mass of the liquid bath and $c_{p_{bath, liq}}$ [J/(°C · kg)] is the enthalpy of the liquid bath. For the **side ledge** control volume, the energy transfer is through melting and freezing of cryolite and heat transfer. The energy transfer related to melting and freezing of cryolite is given by:

$$E_{tc, sol} = w_{fus} c_{p_{cry, sol}} (T_{liq} - T_{sl}). \quad (\text{A.56})$$

$E_{tc, sol}$ [W] is the energy required into the side ledge when frozen cryolite heats from side ledge temperature T_{sl} to liquidus temperature T_{liq} . w_{fus} [kg/s] is given above and $c_{p_{cry, sol}}$ [J/(°C · kg)] is the heat capacity of solid cryolite. The time derivative of the side ledge temperature is given by:

$$\dot{T}_{sl} = \frac{Q_{liq-sl} - Q_{sl-wall} - E_{tc, sol}}{m_{sl} c_{p_{cry, sol}}}. \quad (\text{A.57})$$

\dot{T}_{sl} [°C/s] is the temperature change in the side ledge, Q_{liq-sl} [W] and $Q_{sl-wall}$ [W] is the heat in and out of the side ledge respectively. m_{sl} [kg] is the mass of the side ledge, and $c_{p_{cry, sol}}$ [J/(°C · kg)] is the heat capacity of solid cryolite. There is no mass transfer through the **wall**. Therefore, the only energy transfer through this control volume is through heat transfer. The time derivative of the wall temperature \dot{T}_{wall} [°C/s] is given by:

$$\dot{T}_{wall} = \frac{Q_{sl-wall} - Q_{wall-0}}{m_{wall} c_{p_{wall}}}. \quad (\text{A.58})$$

$Q_{sl-wall}$ [W] is the heat from the side ledge to the wall, Q_{wall-0} [W] is the heat from the wall to the ambient, m_{wall} [kg] is the mass of the wall and $c_{p_{wall}}$ [J/(°C · kg)] is the heat capacity of the wall.

Appendix A.7. Liquidus temperature

In [30], the liquidus temperature T_{liq} was determined for primary crystallization of cryolite (Na_3AlF_6) in a system consisting of the bath components $Na_3AlF_6 - AlF_3 - LiF - CaF_2 - MgF_2 - KF$. The liquidus temperature was determined by thermal analysis in a vertical alumina tube furnace under argon atmosphere. An empirical curve was fitted, which is valid from temperatures $1011^\circ C$ to approximately $800^\circ C$. The curve is given by:

$$\begin{aligned}
T_{liq} = & 1011 + 0.50[AlF_3] - 0.13[AlF_3]^{2.2} \\
& - \frac{3.45[CaF_2]}{1 + 0.0173[CaF_2]} \\
& + 0.124[CaF_2][AlF_3] - 0.00542([CaF_2][AlF_3])^{1.5} \\
& - \frac{7.93[Al_2O_3]}{1 + 0.0936[Al_2O_3] - 0.0017[Al_2O_3]^2 - 0.0023[AlF_3][Al_2O_3]} \\
& - \frac{8.90[LiF]}{1 + 0.0047[LiF] + 0.0010[AlF_3]^2} \\
& - 3.95[MgF_2] - 3.95[KF].
\end{aligned} \tag{A.59}$$

[x] denote the weight-% of component x . In the simulator, it is assumed that the following components are constant at values $[MgF_2] = 1\%$, $[CaF_2] = 5\%$, $[KF] = [LiF] = 0\%$. This yields:

$$\begin{aligned}
T_{liq} = & 991.2 + 1.12[AlF_3] - 0.13[AlF_3]^{2.2} + 0.061[AlF_3]^{1.5} \\
& - \frac{7.93[Al_2O_3]}{1 + 0.0936[AlF_3] - 0.0017[AlF_3]^2 - 0.0023[AlF_3][Al_2O_3]}.
\end{aligned} \tag{A.60}$$

Appendix A.8. Further simplifications in the simulation model

In addition to assumptions and simplifications accounted for in the article, some additional simplifications are made in the simulation model. The reason for this is to simplify the analytical expression in the ODE's used to simulate the dynamics of the simulation model. The ODE's will still describe a complex nonlinear system, but comparing predictive models with the simulation models, and thus analysing the performance of the novel predictive models will be clearer. From the expression for \dot{T}_{bath} in (A.55), the terms E_u , E_{sc} , $E_{r_{Al}}$ and $E_{r_{bath}}$ are omitted. Thus, in the simulation model, the expression for \dot{T}_{bath} is given by:

$$\dot{T}_{bath, sim} = \frac{P_{el} - Q_{bath-sl} - E_{tc, liq}}{m_{bath}c_{p_{bath, liq}}}. \tag{A.61}$$

This neglects some essential physical effects in the process. This is justified by the argument that the main purpose of this work is to evaluate data driven models on a complex nonlinear system, rather than simulating the dynamics of an aluminum electrolysis cell as good as possible.